Thermally-Initiated Formation of Criegee Intermediate CH_2OO in the Oxidation of Ethane

Rizalina T. Saragi,[†] Nathan A. Seifert,[†,‡] Raghu Sivaramakrishnan,[†] and Kirill Prozument[*,†]

[†]*Chemical Sciences and Engineering Division, Argonne National Laboratory, Lemont, IL, 60439, USA*

[‡]*Department of Chemistry and Chemical & Biomedical Engineering, University of New Haven, West Haven, CT 06516, USA*

E-mail: prozument@anl.gov

Abstract

Criegee intermediates (CIs) play an important role in the atmospheric chemistry as a transient source of OH radical, through their formation by the ozonolysis of unsaturated organic compounds. Here, we report thermally initiated formation of the smallest CI (CH_2OO) in the oxidation of ethane (CH_3CH_3) that may be relevant to combustion and flames. The SiO_2/SiC oxidation microreactor is heated to 1800 K and has a short residence time of $\sim$100 μs. The CH_2OO we observe is likely formed in a lower temperature region near the microreactor's exit. Plausible mechanisms for CH_2OO formation and retention at these conditions mediated by methylperoxy (CH_3OO) radicals are discussed. Pure rotational spectra of CH_2OO and other intermediates, HO_2, CH_3CHO, CH_2CHOH, c-CH_2OCH_2, CH_3CH_2CHO, CH_3OOH, and HCOOH are detected with a chirped-pulse Fourier transform millimeter-wave spectrometer operating in the 60–90 GHz frequency range. Detection occurs in a molecular beam where the species are supersonically cooled to 5 K.

Introduction

Criegee intermediates (CIs) are carbonyl oxides with two charge centers on the oxygen atoms. It was shown that in addition to the main, relatively inert, singlet closed-shell zwitterion character, there is an admixture of an exited triplet biradical state that is responsible for the substantial reactivity of CIs.[1] Although Rudolf Criegee initiated research on CIs back in 1949, and proposed their formation in the alkene ozonolysis,[2] it wasn't until 2008 that Taatjes et al. observed the smallest CI, CH_2OO, using tunable synchrotron photoionization with multiplexed mass spectrometry.[3] One of the main techniques now used to obtain CIs and study their reactivity is the reaction between O_2 and CH_2I, which is obtained by the 248 nm photolysis of CH_2I_2.[4–6]

The zwitterionic character of CIs results in a relatively high dipole moment making them convenient for measurement via rotational spectroscopy. Endo and coworkers have been studying various CIs using Fourier transform microwave (FTMW) spectroscopy. They produced CH_2OO by mixing CH_2Br_2 or CH_2I_2 with O_2 in a discharge nozzle, and experimentally determined the molecular structure of CH_2OO.[7,8]

McCarthy et al. demonstrated the formation of CH_2OO from the mixture of CH_4 and O_2 in an electrical discharge.[9] Womack et al. successfully employed FTMW spectroscopy to detect CH_2OO, representing the first observation of this species resulting from the ozonolysis of ethylene.[10] In these and other laboratory studies, the reactive precursors to CIs (CH_3, CH_2I, or O_3) originate from non-thermal energy sources such as electrical discharge or photolysis laser.[7–11] Ozonolysis of alkenes in the atmosphere is now an established source of atmospheric CIs.[12] In those reactions, a vibrationally excited CI can either immediately undergo unimolecular dissociation forming OH, or be stabilized by collisions and react with other atmospheric species.[13] While the role of CI in the atmospheric chemistry is an active field of research,[14] its presence in other gas-phase environments is less studied. In particular, Andersen and Carter suggested that CH_2OO may be formed in dimethyl ether combustion,[15] but no experimental evidence has been found. We query whether a stabilized CI can originate

in a high-temperature thermal environment.

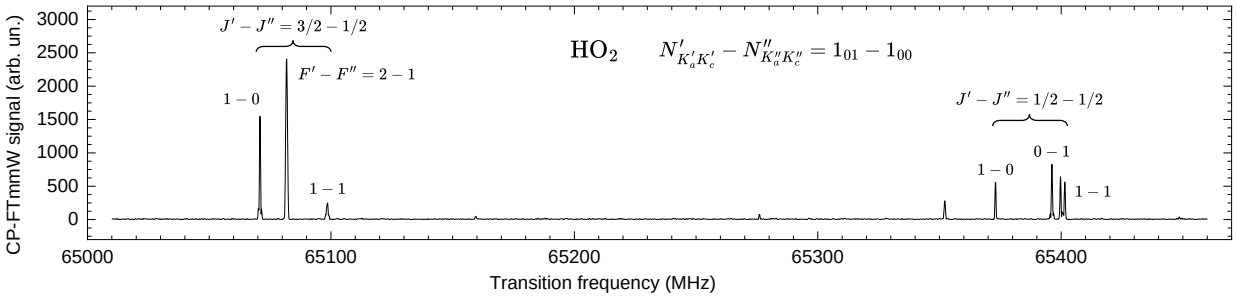

Figure 1: The spectrum of HO_2 produced by the oxidation of ethane. The fine structure of the $1_{01} - 0_{00}$ rotational transition is shown and labeled. The remaining lines are unassigned. The chirp bandwidth is $\Delta\nu = 450$ MHz, and the resultant FID is a 6 s average of 10^6 acquisitions. $\nu_{\mathrm{LO}} = 63$ GHz.

In this study, we observe CH_2OO in a combustion-relevant environment using a custom-built chirped-pulse Fourier transform millimeter-wave (CP-FTmmW)[16–18] spectrometer. CH_2OO emerges from a microreactor heated to the wall temperature $T_{wall} = 1800$ K where the pool of methyl radicals, which we deem the likeliest precursor in CH_2OO formation here, is created. We discuss a) the conditions in the reactor that would prevent complete consumption of CH_2OO before detection and b) the reaction mechanisms that might be responsible for producing CH_2OO from the available building blocks. We also identify other intermediates and infer the mole fractions of CH_2OO, HO_2, CH_3CHO, CH_2CHOH, c-CH_2OCH_2, CH_3CH_2CHO, CH_3OOH, and HCOOH, and compare those to a kinetic model prediction. The observation of CH_2OO product from the oxidation of a simple hydrocarbon such as ethane may provide further important constraints on modeling the reaction networks relevant to practical combustion chemistry, plasma and other radical-initiated oxidations, and other chemically reactive environments that span a wide range of temperatures and pressures such as those in hostile planetary systems like exoplanets.

Results and Discussion

The most abundant detected intermediate in the oxidation of CH_3CH_3 is the HO_2 radical, and its rotational spectrum with fine structure is shown in Fig.1. The spectrum is a Fourier transform of the free induction decay (FID) that accumulates 1 million single FIDs recorded in just 6 seconds. The measured full-width at half-maximum (FWHM) linewidths of about 600 kHz are defined by the Doppler dephasing of the FID in the diverging molecular beam. The spectra of CI CH_2OO and its isomer, formic acid (HCOOH), are shown in Fig.2. We also demonstrate the transitions of vinyl alcohol (CH_2CHOH) and methylhydroperoxide (CH_3OOH) in a single spectrum in Fig.3. Additional lines of these intermediates and spectra of acetaldehyde (CH_3CHO), propanal (CH_3CH_2CHO), and oxirane (c-CH_2OCH_2) are available in the Supporting Information.

Using the published dipole moments and rotational constants of HO_2 (μ_a=1.412 D, μ_b=1.541 D),[19,20] *syn*-CH_2CHOH (μ_a=0.616 D, μ_b=0.807 D),[21,22] *anti*-CH_2CHOH (μ_a=0.547 D, μ_b=1.702 D),[23]CH_3OOH (μ_a=0.606 D, μ_b=0.071 D),[24] CH_2OO (μ_a=5.0 D),[25] CH_3CHO (μ_a= 2.53, μ_b = 1.07), the average values of two works,[26,27] c-CH_2OCH_2 (μ_b = 1.89 D),[28] CH_3CH_2CHO (μ_a= 1.71, μ_b = 1.85),[29] *trans*-HCOOH (μ_a= 1.421, μ_b = 0.21),[30] and *cis*-HCOOH (μ_a= 2.65, μ_b = 2.71),[31] we employ the PGOPHER program[32] to simulate line intensities, assuming a rotational temperature of 5 K. The mole fractions of these intermediates are obtained by comparing their line intensities to that of a benchmark molecule, $CH_2DC^{13}CH$ (μ_a=0.7818 D),[33–35] with a known mole fraction. A sample of 5% propyne in argon flows at $Q = 2000$ sccm through the SiO_2/SiC reactor at $T_{wall} = 1500$ K to minimize propyne pyrolysis and maintain the conditions similar to those in the oxidation measurements. We measure the $4_{04} - 3_{03}$ transition of $CH_2DC^{13}CH$ (Fig. S6), which is contained in the sample in natural abundance at 7.69×10^{-8} mole fraction.

The measured mole fractions are compared to a simulation performed with an in-house kinetics model, ThInK,[36–39] developed predominantly using high-level theoretical methods to describe the combustion of small hydrocarbons (Table 1). This model currently includes

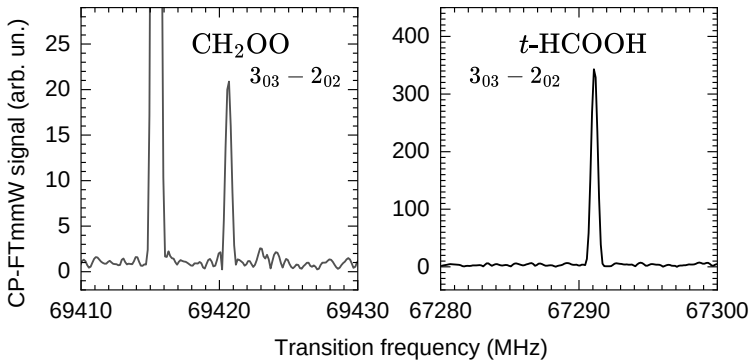

Figure 2: Two CH_2O_2 isomers in the oxidation of ethane. Left panel: the $3_{03} - 2_{02}$ transition of Criegee intermediate, CH_2OO. The spectrum is obtained with a $\Delta\nu = 150$ MHz excitation chirp, only a 20 MHz portion is shown. The spectrum is a Fourier transform of an FID that is averaged 10^8 times in 10 min. $\nu_{LO} = 67.2$ GHz. Right panel: the $3_{03} - 2_{02}$ transition of formic acid, *trans*-HCOOH. The chirp bandwidth is 20 MHz and the FID is averaged 10^7 times in 1 min. $\nu_{LO} = 65.2$ GHz

160 species and 1090 elementary reactions. A Chemkin[40] interpreted output of this model, obtained using a 0-D homogeneous reactor approximation, is provided in the SI. The abundances in the simulation at the wall temperature conditions are provided here merely as a qualitative indicator for the intermediates observed in the present experiments. For example, the key species of interest here, CH_2OO, is not included in the present model or any other literature chemical kinetic model for high-temperature chemistry, and therefore, there is no entry for this species from the simulation. The SI also provides analyses of the pathways responsible for the observed intermediates from the simulations.

Oxidation of CH_3CH_3 is initiated at a high temperature, and both the unimolecular dissociation of ethane

$$CH_3CH_3 \longrightarrow 2\,CH_3 \tag{1}$$

and its oxidation

$$CH_3CH_3 + O_2 \longrightarrow CH_3CH_2 + HO_2 \tag{2}$$

Table 1: The experimental and simulated abundances of the ethane oxidation intermediates. The experimental abundance of CH_2CHOH includes 79% *syn*- and 21% *anti*- conformers, CH_3OOH includes 88% 0^+ and 12% 0^- tortional ground state tunneling levels, the HCOOH includes 97.5% *trans*- and 2.5% *cis*- conformers. The experimental uncertainty of the mole fraction determinations is ±30% of the values. The ThInK kinetic model prediction is for T = 1800 K, p = 1 atm, and t = 100 μs.

Species	Experiment	Kinetic model
CH_3CHO	5.77×10^{-6}	1.44×10^{-5}
CH_2CHOH	2.56×10^{-6}	9.34×10^{-6}
c-CH_2OCH_2	4.54×10^{-7}	2.20×10^{-5}
CH_3CH_2CHO	1.49×10^{-6}	3.17×10^{-7}
HO_2	1.60×10^{-5}	1.54×10^{-5}
CH_3OOH	5.01×10^{-7}	4.37×10^{-14}
CH_2OO	5.85×10^{-9}	–
HCOOH	3.74×10^{-7}	2.51×10^{-10}

contribute to the initial pool of radicals. This initial pool of radicals, CH_3, C_2H_5, and HO_2, rapidly undergo chain branching and other oxidation reactions as well as dissociation (in the case of C_2H_5 and HO_2) at T_{wall} = 1800 K to rapidly generate more reactive atoms/radicals such as H, O, and OH. These reactive species then rapidly catalyze the destruction of C_2H_6 via bimolecular abstractions and initiate secondary chemistry. As many as 57 stable species and radicals are formed with mole fractions > 0.1 ppm within a 10 μs timescale as indicated by simulations using our in-house model. Figure S7 depicts the time evolution of a small sub-set of key stable species and radicals at 1800 K and 1 atm. Figure S8 demonstrates that while (R2) initially has the greatest rate of HO_2 production, it is surpassed by the $C_2H_5 + O_2 \longrightarrow C_2H_4 + HO_2$ channel at 1 μs. At the time of measurement (100 μs), the $HCO + O_2 \longrightarrow HO_2 + CO$ reaction is the dominant source of HO_2. Here we would like to focus on the chemistry responsible for the key intermediates observed here, and in particular hypothesize the sources for the elusive Criegee species, CH_2OO, detected in this work.

Reaction of methyl radical (CH_3) with O_2 proceeds through a chemically activated complex CH_3OO^*, which could be stabilized

$$CH_3 + O_2 \longrightarrow CH_3OO \tag{3}$$

or lead to $CH_3O + O$ or $CH_2O + OH$.[41] We are observing multiple strong lines that match the prediction for CH_3OO by Endo.[42] The stabilized methylperoxy (CH_3OO) may also undergo multichannel reactions.[43] One route is the production of methylhydroperoxide (CH_3OOH) via a CH_3OO and HO_2 reaction.[43,44] The mechanism is initiated by a barrierless formation of a diradical hydrogen-bonded complex, $CH_3OO\cdots HO_2$, stabilized by approximately 4.5 kcal/mol. The reaction pathways occur both on the triplet and singlet potential energy surfaces (PESs). The main reaction pathway occurs on the triplet PES and proceeds through a submerged barrier to the CH_3OOH and O_2 products:[45,46]

$$CH_3OO + HO_2 \longrightarrow CH_3OO\cdots HO_2 \longrightarrow CH_3OOH + O_2. \tag{4}$$

Additional sources for CH_3OOH are other radical-radical reactions such as $CH_3OO + CH_3O$ and direct hydrogen abstraction by CH_3OO from the reactant C_2H_6. Interestingly, the simulations using the model at 1800 K do not predict CH_3OOH to be formed even in sub-ppm levels (Table 1). This is not surprising since the O–O bond energy $BDE_{298} = 44.6$ kcal/mol[47,48] and at $T > 1000$ K dissociation to $CH_3O + OH$ is facile.[49] However as discussed below, the detection of CH_3OOH and CH_2OO is due to the complex flow fields[50,51] within this microreactor leading to wide temperature and pressure distributions.

Observation of CH_2OO originating from a high-temperature environment is important because of its high reactivity[14] and a possible role it may play in combustion and flames. At the same time, the measurements by Stone et al. of CH_2OO unimolecular decomposition at temperatures 450–650 K and the deduced rate expression[52] suggest that this CI would be extremely short-lived at the 1500–1800 K temperatures inside our reactor. Their prediction for the rate of decomposition at 1500 K, 1 bar would be $10^7 - 10^8$ s^{-1}. Assuming, for a moment, a uniform pressure and temperature distribution within the reactor, and an estimated residence time of $\sim$100 μs,[53] CH_2OO would be practically not detectable. However, there are temperature and pressure gradients within the reactor;[50,51] therefore, it is plausible

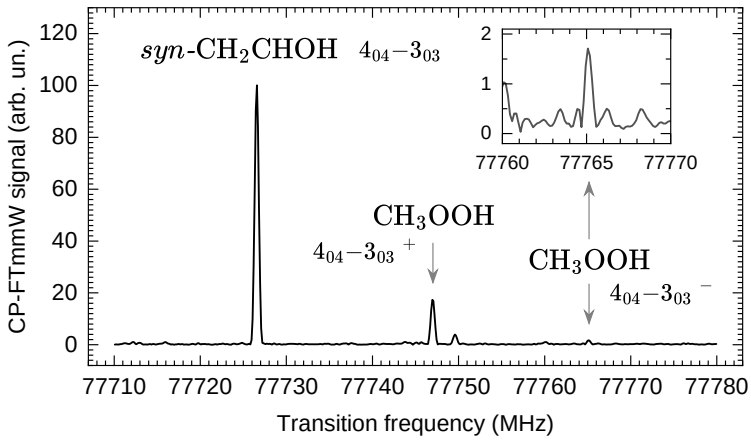

Figure 3: Vinyl alcohol and methylhydroperoxide in the oxidation of ethane. The $4_{04} - 3_{03}$ transitions of *syn*-CH_2CHOH and CH_3OOH are shown. The transition within the "–" torsional state of CH_3OOH is magnified in the insert. The frequency of the excitation pulse is chirped from 77780 to 77710 MHz, and the FID is averaged 10^9 times in 1 h and 40 min. With that significant averaging, a slightly increased noise level near the red end of the spectrum is due to the chirp leakage into the FID detection time window. $\nu_{LO} = 75.8$ GHz.

that the CI is formed from the available free radicals and molecules in a colder region at the central axis of the reactor,[54] or near the extraction region. At the end of the reactor, the temperature drops and eventually reaches 5 K in the supersonic expansion, where collisions cease and detection occurs. For example, it would be reasonable to assume that the intermediates formed by the oxidation of ethane in the high-temperature region of the reactor proceed to its exit where they briefly encounter an area of 650 K for which the measured[52] rate of CH_2OO decomposition is 1.2×10^4 s^{-1}. Most of CH_2OO formed and stabilized in that 650 K zone or anywhere in a colder area down the stream will avoid isomerization or unimolecular decomposition[55] and would be detectable.

Under such colder (relative to T_{wall}) conditions there could be multiple mechanistic postulates for the formation of CH_2OO. For example, the chemical environment in the microreactor is akin to that experienced during radical-initiated oxidations of hydrocarbons. In such a scenario, we have shown in recent theory/modeling work on ethane oxidation[43] that reactions not considered in hydrocarbon autoignition come into prominence. One such example is the reaction of peroxy radicals with OH. This reaction has been the subject of

recent atmospheric chemical kinetics studies.[56] In traditional auto-ignition scenarios, peroxy radicals undergo subsequent oxidation to produce OH and therefore, peroxy and OH radicals do not co-exist in significant concentrations to permit cross-reactions. However, in radical-initiated oxidations in the presence of an external radical source, the inclusion of this multi-channel radical-radical reaction can influence auto-ignition in hydrocarbons.[43] Total rate coefficients for CH_3O_2 + OH are fast ($\sim 10^{-10}$ cm^3 molecule^{-1} s^{-1}) and therefore even a small flux into the CH_2OO + H_2O product channel can lead to noticeable formation of CH_2OO at exit conditions in the microreactor. However, the reaction is exothermic by 45 kcal/mol,[47,48] which probably leads to prompt isomerization or dissociation[57] of CH_2OO. The present simulations using the model at 1800 K indicate that copious amounts of H- and O-atoms are also formed (Fig. S7). Direct abstractions of CH_3OO by these reactive atoms can also be sources for the observed CH_2OO. Such reactions may also be facile but their analysis requires the use of high-level multi-reference methods.[58]

The theoretical investigation of the discharge-initiated formation of CH_2OO in a mixture of CH_4 and O_2 conducted by Nguyen, McCarthy, and Stanton puts forward another chemical mechanism that may be applicable to the present study.[44] Under the discharge conditions,[9] the reaction is initiated by the methyl radicals from the C−H bond cleavage in CH_4. In our experiment, the source of methyl radical is initially the simple bond fission in CH_3CH_3 (Reaction 1), and later the $C_2H_5 + H \longrightarrow CH_3 + CH_3$ reaction (Fig. S9). Following the mechanism proposed by Nguyen et al., methyl radicals react with O_2 to form vibrationally excited methylperoxy, CH_3OO^*, which immediately reacts with another O_2, skipping[59] thermalization:

$$CH_3 + 2\,O_2 \longrightarrow CH_3OO^* + O_2 \longrightarrow CH_2OO + HO_2. \tag{5}$$

The H-atom abstraction by O_2 to form CH_2OO encounters a much lower barrier of 9.7 kcal/mol than if the methylperoxy had stabilized in its potential well by collisions.[44,60] The

CH_2OO formed with vibrational energy below the 12.1 kcal/mol barrier (relative to the reactants in R5) to isomerization to dioxirane (*cyc*-CH_2OO) is preserved, cooled and becomes available for detection.[44] We do not observe rotational lines of dioxirane[61] either because there is not enough CH_2OO that is sufficiently energized or due to a well-skipping isomerization of *cyc*-CH_2OO to formic acid (HCOOH). Formic acid is observed in this work (Fig.2) at the level, which exceeds the kinetic model prediction by a factor of 10^3 (Table 1). It remains to be determined what fraction of the observed HCOOH is mediated by CH_2OO.

A recently published work by Qian et al. demonstrates a much slower rate of CH_2OO unimolecular decomposition than what would be predicted by the statistical theory.[11] In their study, specific vibrational modes of CH_2OO are excited and the inhibited dissociation is associated with the sparse vibrational level structure and poor IVR, which is necessary to reach the transition state. How is the internal energy of CH_2OO forming through (R5) distributed among its degrees of freedom? The vibrational population distribution of a reaction product is generally non-Boltzmann and encodes the overlap between its equilibrium geometry and the configuration that its nuclei had in the transition state.[62] The energy in a nascent reaction product may be preferentially deposited into a specific vibrational mode that is reminiscent of the nuclear motion that promoted the reaction.[63] We speculate that if energy flow out of such a mode in the nascent CH_2OO in (R5) is ineffective, the CI may avoid isomerization or dissociation and be more readily stabilized by collisions even if its available energy is above the barriers to those transformations.

The mechanism of (R5) described by Nguyen et al. includes rapid formation of an intermediate van der Waals complex $O_2 \cdots CH_3OO^*$ and tunneling under the 9.7 kcal/mol barrier to $HO_2 + CH_2OO$ on the time scales relevant to our experiment. For example, with only 0.5 kcal/mol of energy above the reactants in (R5), the $O_2 \cdots CH_3OO^*$ complex reacts in $\sim$1 μs.[44]

Related to that mechanism, some radical–molecule pairs react faster below 200 K because they form weakly bound complexes that have long enough lifetime for tunneling through

the barrier to complete.[64–66] Although Nguyen et al. do not show a negative temperature dependence of the rate constant for (R5) in their energy range, it would be interesting to test that possibility for a cooled $O_2 \cdots CH_3OO$ complex. We also point to a possibility of the roaming mechanism[67] facilitating (R5) by sampling multiple mutual orientations of O_2 and CH_3OO to find the transition state.

In summary, the observation of CH_2OO exiting the hot reactor is unexpected because of its predicted extremely short lifetime at 1800 K. We conclude that the CH_2OO we detect is forming in a cooler ($T \leq 650$ K) region near the exit from the reactor where the temperature rapidly drops to 5 K in the expansion region. Mechanistic postulates for the formation of CH_2OO include the reaction of CH_3OO + OH[43,56] or the non-thermal mechanism involving CH_3OO^* + O_2.[44] The upgraded Argonne E-band chirped-pulsed millimeter-wave spectrometer demonstrates high sensitivity with deep averaging of the molecular FID.

This work suggests that the reactive Criegee intermediates may be important in the intermediate-temperature (up to $\sim$ 1000 K) environments in addition to the atmosphere. They may also be formed in radical initiated oxidations that can lead to situations where peroxy radicals can co-exist with reactive atoms/radicals such as OH, H, or O-atoms. Future experiments to validate the non-thermal mechanism (R5) may include deuteration of ethane to gauge the role of tunneling in this CH_2OO formation. Dimethyl ether with its slightly lower CH_3O-CH_3 bond dissociation energy (BDE_{298} = 84.1 kcal/mol) than ethane's CH_3-CH_3 (BDE_{298} = 90.1 kcal/mol)[47,48] would be a better source of methyl radicals and thus a possibility of CH_2OO formation in its oxidation is of interest. Detection of larger CIs in a similar experiment would be challenging due to the increased rotational partition function reducing the line intensities, but not impossible. A Criegee-mediated pathway to formic acid and the consecutive chemistry of stabilized CH_2OO at intermediate temperatures may be investigated with a combined modeling-experiment-theory[68] approach.

Methods

Reactor and gas handling system

The SiO_2/SiC reactor is constructed of a quartz tube (0.8 mm i.d., 1.0 mm o.d., VitroCom, p/n CV8010) inserted into a 60 mm-long SiC tube (1.0 mm i.d., 1.95 mm o.d., Saint-Gobain Ceramics, Hexoloy SE, p/n 3238672). The gap between the two tubes is sealed by vacuum epoxy near the entrance of the reactor to contain the flow of the ethane and oxygen mixture within the SiO_2 insert and minimize deterioration of the SiC heater tube. After annealing, the quartz insert is making a thermal contact with the SiC tube, which is resistively heated to $T_{\text{wall}} = 1800$ K (the maximal temperature along the wall detected by an optical pyrometer)[69] during measurements. The oxidation of CH_3CH_3 is initiated and the secondary chemistry evolves during the ~ 100 µs residence time within the reactor. The oxidation intermediates, including CH_2OO, are captured by the CP-FTmmW spectrometer once the gas has expanded supersonically from the reactor into the vacuum chamber and cooled to $T_{\text{rot}} \approx 5$ K.

The gas delivery and vacuum systems are described in a prior publication.[70] Briefly, the mixture of 5% CH_3CH_3 and 5% O_2 mole fractions in Ar is produced by merging the flows of 1) CH_3CH_3 at 100 sccm, 2) neat Ar at 900 sccm, and 3) mixture of 10% O_2 in Ar at 1000 sccm, and directed to the reactor at $Q = 2000$ sccm combined flow rate. The reactor operates in a continuous flow regime. When the reactor is heated to $T_{\text{wall}} = 1800$ K, the stagnation pressure becomes $p_0 = 1.6$ bar. At these conditions, the pressure in the chamber is $p_{\text{ch}} = 1.5 \times 10^{-2}$ mbar maintained by two turbomolecular pumps. Gasses are purchased from Airgas and have the following stated purity. Ethane is Research grade 99.99% (p/n ET R80) with the total hydrocarbon impurity (THC) of ≤ 80 ppm. Neat argon is Research Plus grade 99.9999% (p/n AR RP300) with THC ≤ 0.1 ppm. The 10% oxygen in argon mixture (p/n X02AR90C3002555) contains Ultra High Purity 99.994% oxygen with THC ≤ 0.5 ppm, and Ultra High Purity 99.999% argon with THC ≤ 0.5 ppm. The THC of the resulting mixture is ≤ 4.3 ppm.

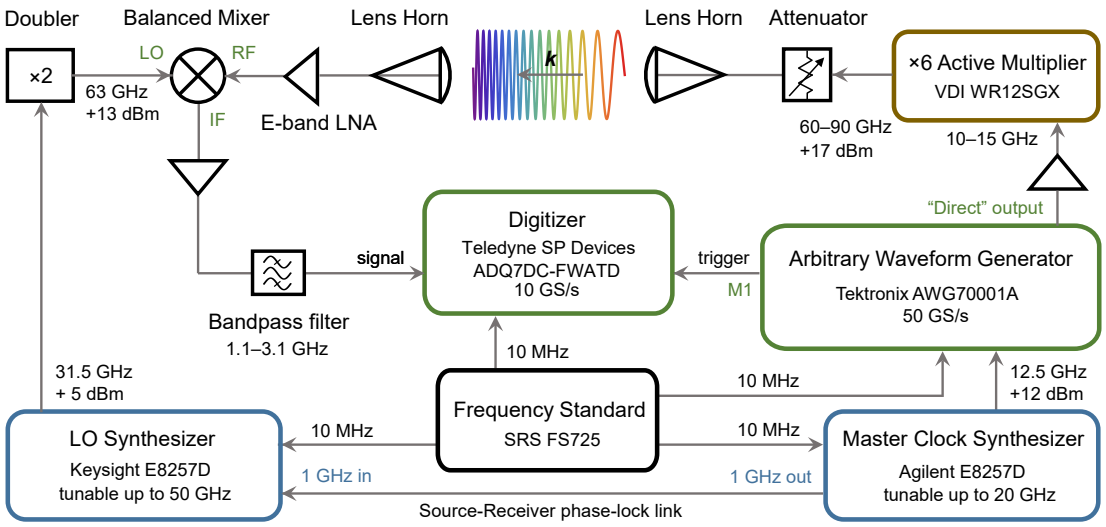

Figure 4: Schematic of the E-band CP-FTmmW spectrometer that utilizes a fast digitizer to record and average the FID. The available frequency range for chirping (60–90 GHz) is indicated and chirps with bandwidths up to $\Delta\nu = 1.2$ GHz (Fig. S2) are utilized. The LO frequency (ν_{LO}) can be set within the same frequency region (60–90 GHz). An example of $\nu_{\mathrm{LO}} = 63$ GHz used to obtain the spectrum in Fig.1 is shown. The direction of the wavevector $\boldsymbol{k}$ of the frequency-chirped, linearly polarized mmW beam propagating between the two lens horn antennas is shown with an arrow.

CP-FTmmW spectrometer

In this work we implement an E-band (60–90 GHz) CP-FTmmW spectrometer with deep averaging of the FID signal using a fast digitizer (ADQ7DC FWATD, PCIe card, by Teledyne SP Devices) inspired by work of Hays et al.[71] The main architecture of the spectrometer remains that of our E-band CP-FTmmW setup, which was described elsewhere.[69]

The schematic of the present spectrometer is shown in Fig.4. Chirped pulses (chirps) are formed by the arbitrary waveform generator (AWG, Tektronix AWG70001A, 50 Gs/s), which is disciplined by a 12.5 GHz clock frequency from the Master Clock Synthesizer (Agilent Technologies, PSG Analogue Signal Generator E8257D, 250 kHz – 20 GHz), and amplified by 14 dB (Marki Microwave, AP-125EQP, 1–25 GHz). The chirps are frequency-multiplied by a factor of 6 and amplified to 16.2–17.8 dBm (42–60 mW) throughout the E band using the Virginia Diode signal generator extension (SGX) module WR12SGX. The last element in the SGX is a passive multiplier, which minimizes the SGX emission during FID detection.

A direct reading manual attenuator (QuinStar QAD-E00000) tunable between 0 and 60 dB attenuation is installed after the SGX for calibration purposes (see the SI). The millimeter-wave (mmW) beam is broadcast to the vacuum chamber by a lens horn antenna (Flann Microwave 26810-NB-17349, 75 mm lens diameter, 33 dBi gain) where it crosses the molecular beam at 90°. RF absorbing sheets (Laird Technologies EMI, p/n 78820181) are placed inside the chamber to dampen stray mmW radiation. On the other side of the chamber, the molecular FID is received by another lens horn antenna, amplified by an E-band low-noise amplifier (LNA, Mi-Wave 955EF-25/8/387, 25 dB gain, 4.5 dB noise figure) and directed to the RF port of the passive balanced mixer (QuinStar QMB-FBFBES, 0.1–5 GHz IF) for frequency downconversion. The mixer is driven by a local oscillator (LO) with a frequency set between 60 and 90 GHz that is provided by a frequency-doubled output of the tunable LO Synthesizer (Keysight, PSG Analogue Signal Generator E8257D, 250 kHz – 50 GHz). The downconverted FID from the IF port of the mixer is amplified (Miteq LNA-40-00100600-18-15P, 45 dB gain, 0.1–6 GHz) and cleaned by a 1.1–3.1 GHz bandpass filter (Lorch Microwave, 10BP7-2100/2200-S). After that, the amplitude of a single FID, which is usually dominated by the noise, fills the digitizer's vertical scale of 1 V_{pp} without exceeding it. The noise floor is set by the mmW LNA. The LO Synthesizer is phase-locked to the Master Clock Synthesizer via a 1 GHz link to maintain the phase stability of the spectrometer. This supplements the 10 MHz frequency standard provided to the synthesizers, AWG, and the ADQ7DC digitizer. As in the segmented chirp scheme,[72] we set the LO frequency (ν_{LO}) close to a relatively narrow chirping region ($\Delta\nu$) covering molecular transitions of interest to keep the IF frequency within the digitizer bandwidth of 3 GHz, but also below a strong digitizer spurious signal[73] (spur) at 2.5 GHz.

The ADQ7 digitizer has a 10 GS/s sampling rate, 3 GHz analogue bandwidth, and 14-bit vertical digitization depth. Although the bandwidth of the digitizer is lower than that of high-end oscilloscopes, it sustains orders of magnitude faster data flow and processing. That allows acquisition of FIDs every 6 µs or with 167 kHz repetition rate. The data flow in the

spectrometer is structured as follows. The AWG is programmed to continuously output a sequence of data frames of 6 µs length that contains a frequency-chirped pulse (chirp) of 0.5 µs duration in the beginning and zeros elsewhere. These data frames stem from the main AWG channel with 8 bit vertical resolution and 50 GS/s sampling rate. A 1-bit marker channel of the AWG provides a trigger to the ADQ7DC digitizer 0.4 µs after the end of the chirp. At that time, the frequency-downconverted FID is recorded by the digitizer for 4 µs. The 0.4 µs delay is for the transient ringing in the downconversion electronics excited by the intense chirp to subside before a much weaker FID is digitized.[18] 2×10^5 consecutive FIDs are averaged within the digitizer before the resulting FID is transferred to a file on the computer that hosts the PCIe card with ADQ7DC. 5000 of these aggregated time traces may be recorded in 1 h and 40 min and then co-added to form a final, 10^9 average FID. However, it is more practical to average between 10^6 (6 s acquisition time) and 10^8 (10 min acquisition time) FIDs. Deep averaging in a reasonable time is achievable due to the combination of the 75% duty cycle of the spectrometer (considering the chirp and the FID duration as a useful time) and a steady (non-pulsed) molecular sample.[74–76] The final frequency domain CP-FTmmW signal (spectrum) is the magnitude of the Fourier transformation of the FID after applying a Kaiser-Bessel window function.

Acknowledgement

The authors are grateful to Stephen Klippenstein for his advice on the CH_2OO chemistry. We thank Yasuki Endo for providing the linelist for methyl peroxy (CH_3OO) radical. This material is based on work supported by the U.S. Department of Energy, Office of Science, Office of Basic Energy Sciences, Division of Chemical Sciences, Geosciences, and Biosciences under contract No. DE-AC02-06CH11357.

Supporting Information Available

The Supporting Information is available free of charge on the ACS Publications website at DOI: 10.1021... Table S1 lists the line assignments, frequencies, and calibrated intensities for the reaction intermediates and the $CH_2DC^{13}CH$ benchmark molecule. Figure S1 shows the the spectra of the $3_{13} - 2_{12}$, $3_{12} - 2_{11}$, and $4_{14} - 3_{13}$ transitions of CH_2OO observed in addition to the $3_{03} - 2_{02}$ line shown in Fig.2. Figure S2 shows a 1200-MHz wide spectrum that contains the lines of CH_3CHO, *syn*-CH_2CHOH, CH_3OOH, and *syn*-CH_3CH_2CHO. The spectral data for Fig. S2 is available in the SI. Figures S3–S5: spectra of *trans*-HCOOH, *cis*-HCOOH, and *c*-CH_2OCH_2. Fig. S6 shows the $4_{04} - 3_{03}$ transition of $CH_2DC^{13}CH$, which is detected in natural abundance and used to deduce the mole fractions of the reaction intermediates. Fig. S7 shows the mole fraction simulations for CH_3CH_3, O_2, HO_2, CH_3, CH_3CH_2, OH, H, O, HCO, CH_2O, CH_3O, CH_3CHO, CH_2CHOH, *c*-CH_2OCH_2, HCOOH, CH_3OO, CH_3OOH, CH_3CH_2CHO, CH_3CH_2OO, and CH_2CH_2OOH. Figs. S8–S24 show the rate of production simulations for HO_2, CH_3, CH_3CH_2, OH, H, O, HCO, CH_2O, CH_3CHO, CH_2CHOH, *c*-CH_2OCH_2, HCOOH, CH_3OO, CH_3OOH, CH_3CH_2CHO, CH_3CH_2OO, and CH_2CH_2OOH. For each species in Figs. S8–S24, up to 10 most contributing to their formation reactions are shown over the initial 5 μs and 200 μs time intervals. The output summary and the detailed results of this kinetic modeling are available as separate files.

References

(1) Miliordos, E.; Xantheas, S. S. The Origin of the Reactivity of the Criegee Intermediate: Implications for Atmospheric Particle Growth. *Angew. Chem. Int. Ed.* **2016**, *55*, 1015–1019.

(2) Criegee, R. Mechanism of Ozonolysis. *Angew. Chem. Int. Ed. Engl.* **1975**, *14*, 745–752.

(3) Taatjes, C. A.; Meloni, G.; Selby, T. M.; Trevitt, A. J.; Osborn, D. L.; Percival, C. J.;

Shallcross, D. E. Direct Observation of the Gas-Phase Criegee Intermediate (CH_2OO). *J. Am. Chem. Soc.* **2008**, *130*, 11883–11885.

(4) Welz, O.; Savee, J. D.; Osborn, D. L.; Vasu, S. S.; Percival, C. J.; Shallcross, D. E.; Taatjes, C. A. Direct Kinetic Measurements of Criegee Intermediate (CH_2OO) Formed by Reaction of CH_2I with O_2. *Science* **2012**, *335*, 204–207.

(5) Beames, J. M.; Liu, F.; Lu, L.; Lester, M. I. Ultraviolet Spectrum and Photochemistry of the Simplest Criegee Intermediate CH_2OO. *J. Am. Chem. Soc.* **2012**, *134*, 20045–20048.

(6) Su, Y.-T.; Huang, Y.-H.; Witek, H. A.; Lee, Y.-P. Infrared Absorption Spectrum of the Simplest Criegee Intermediate CH_2OO. *Science* **2013**, *340*, 174–176.

(7) Nakajima, M.; Endo, Y. Communication: Determination of the molecular structure of the simplest Criegee intermediate CH_2OO. *J. Chem. Phys.* **2013**, *139*, 101103.

(8) Nakajima, M.; Yue, Q.; Li, J.; Guo, H.; Endo, Y. An experimental and theoretical study on rotational constants of vibrationally excited CH_2OO. *Chem. Phys. Lett.* **2015**, *621*, 129–133.

(9) McCarthy, M. C.; Cheng, L.; Crabtree, K. N.; Martinez, O. J.; Nguyen, T. L.; Womack, C. C.; Stanton, J. F. The Simplest Criegee Intermediate ($H_2C{=}O{-}O$): Isotopic Spectroscopy, Equilibrium Structure, and Possible Formation from Atmospheric Lightning. *J. Phys. Chem. Lett.* **2013**, *4*, 4133–4139.

(10) Womack, C. C.; Martin-Drumel, M.-A.; Brown, G. G.; Field, R. W.; McCarthy, M. C. Observation of the simplest Criegee intermediate CH_2OO in the gas-phase ozonolysis of ethylene. *Sci. Adv.* **2015**, *1*, e1400105.

(11) Qian, Y.; Nguyen, T. L.; Franke, P. R.; Stanton, J. F.; Lester, M. I. Nonstatistical

Unimolecular Decay of the CH_2OO Criegee Intermediate in the Tunneling Regime. *J. Phys. Chem. Lett.* **2024**, *15*, 6222–6229.

(12) Khan, M. A. H.; Percival, C. J.; Caravan, R. L.; Taatjes, C. A.; Shallcross, D. E. Criegee intermediates and their impacts on the troposphere. *Environ. Sci.: Processes Impacts* **2018**, *20*, 437–453.

(13) Lester, M. I.; Klippenstein, S. J. Unimolecular Decay of Criegee Intermediates to OH Radical Products: Prompt and Thermal Decay Processes. *Acc. Chem. Res.* **2018**, *51*, 978–985.

(14) Chhantyal-Pun, R.; Khan, M. A. H.; Taatjes, C. A.; Percival, C. J.; Orr-Ewing, A. J.; Shallcross, D. E. Criegee intermediates: production, detection and reactivity. *Int. Rev. Phys. Chem.* **2020**, *39*, 385–424.

(15) Andersen, A.; Carter, E. A. Hybrid Density Functional Theory Predictions of Low-Temperature Dimethyl Ether Combustion Pathways. II. Chain-Branching Energetics and Possible Role of the Criegee Intermediate. *J. Phys. Chem. A* **2003**, *107*, 9463–9478.

(16) Brown, G. G.; Dian, B. C.; Douglass, K. O.; Geyer, S. M.; Shipman, S. T.; Pate, B. H. A broadband Fourier transform microwave spectrometer based on chirped pulse excitation. *Rev. Sci. Instrum.* **2008**, *79*, 053103.

(17) Park, G. B.; Steeves, A. H.; Kuyanov-Prozument, K.; Neill, J. L.; Field, R. W. Design and evaluation of a pulsed-jet chirped-pulse millimeter-wave spectrometer for the 70–102 GHz region. *J. Chem. Phys.* **2011**, *135*, 024202.

(18) Steber, A. L.; Harris, B. J.; Neill, J. L.; Pate, B. H. An arbitrary waveform generator based chirped pulse Fourier transform spectrometer operating from 260 to 295 GHz. *J. Mol. Spectrosc.* **2012**, *280*, 3–10.

(19) Saito, S.; Matsumura, C. Dipole moment of the HO_2 radical from its microwave spectrum. *J. Mol. Spectrosc.* **1980**, *80*, 34–40.

(20) Beers, Y.; Howard, C. J. The microwave spectrum of HO_2 near 65 GHz. *J. Chem. Phys.* **1975**, *63*, 4212–4216.

(21) Saito, S. Microwave spectroscopic detection of vinyl alcohol, CH_2=CHOH. *Chem. Phys. Lett.* **1976**, *42*, 399–402.

(22) Melosso, M.; McGuire, B. A.; Tamassia, F.; Degli Esposti, C.; Dore, L. Astronomical Search of Vinyl Alcohol Assisted by Submillimeter Spectroscopy. *ACS Earth Space Chem.* **2019**, *3*, 1189–1195.

(23) Rodler, M. Microwave spectrum, dipole moment, and structure of anti-vinyl alcohol. *J. Mol. Spectrosc.* **1985**, *114*, 23–30.

(24) Tyblewski, M.; Ha, T.; Meyer, R.; Bauder, A.; Blom, C. E. Microwave and millimeter-wave spectra, electric dipole moment, and internal rotation effects of methyl hydroperoxide. *J. Chem. Phys.* **1992**, *97*, 6168–6180.

(25) Daly, A. M.; Drouin, B. J.; Yu, S. Submillimeter measurements of the Criegee intermediate CH_2OO, in the gas phase. *J. Mol. Spectrosc.* **2014**, *297*, 16–20.

(26) Bossert, W.; Ekkers, J.; Bauder, A.; Günthard, H. H. Stark effect and isometric groups of nonrigid molecules.: I. General theory and determination of the relative signs of components of the electric dipole moment of semirigid molecules with one and two symmetric rotors. *Chem. Phys.* **1978**, *27*, 433–463.

(27) Turner, P. H.; Cox, A. P. Microwave spectrum, structure, dipole moment and centrifugal distortion of nitrosomethane. Dipole moment of acetaldehyde. *J. Chem. Soc., Faraday Trans. 2* **1978**, *74*, 533–559.

(28) Cunningham Jr, G. L.; Boyd, A.; Myers, R. J.; Gwinn, W. D.; Le Van, W. The microwave spectra, structure, and dipole moments of ethylene oxide and ethylene sulfide. *J. Chem. Phys.* **1951**, *19*, 676–685.

(29) Butcher, S. S.; Wilson, E. B. Microwave Spectrum of Propionaldehyde. *J. Chem. Phys.* **1964**, *40*, 1671–1678.

(30) Minowa, T.; Matsuo, Y.; Kuze, H.; Shimizu, T. Measurement and calculation of rotational relaxation rate constants in the ground and excited vibrational states of HCOOH. *J. Chem. Phys.* **1983**, *78*, 1861–1866.

(31) Hocking, W. H. The Other Rotamer of Formic Acid, *cis*-HCOOH. *Z. Naturforsch. A* **1976**, *31*, 1113–1121.

(32) Western, C. M. PGOPHER: A program for simulating rotational, vibrational and electronic spectra. *J. Quant. Spectrosc. Radiat. Transf.* **2017**, *186*, 221–242.

(33) Leguennec, M.; Demaison, J.; Wlodarczak, G.; Marsden, C. Rotational Spectra of $CH_2DC{\equiv}CH$ and $CH_3C{\equiv}CD$: Experimental and ab Initio Equilibrium Structures of Propyne. *J. Mol. Spectrosc.* **1993**, *160*, 471–490.

(34) Endres, C. P.; Schlemmer, S.; Schilke, P.; Stutzki, J.; Müller, H. S. The Cologne Database for Molecular Spectroscopy, CDMS, in the Virtual Atomic and Molecular Data Centre, VAMDC. *J. Mol. Spectrosc.* **2016**, *327*, 95–104.

(35) The Cologne Database for Molecular Spectroscopy (CDMS). Available at `https://cdms.astro.uni-koeln.de` (accessed on 30 October 2024).

(36) Krisman, A.; Mounaïm-Rousselle, C.; Sivaramakrishnan, R.; A. Miller, J.; H. Chen, J. Reference natural gas flames at nominally autoignitive engine-relevant conditions. *Proc. Combust. Inst.* **2019**, *37*, 1631–1638.

(37) Klippenstein, S. J. From theoretical reaction dynamics to chemical modeling of combustion. *Proc. Combust. Inst.* **2017**, *36*, 77–111.

(38) Miller, J. A.; Sivaramakrishnan, R.; Tao, Y.; Goldsmith, C. F.; Burke, M. P.; Jasper, A. W.; Hansen, N.; Labbe, N. J.; Glarborg, P.; Zádor, J. Combustion chemistry in the twenty-first century: Developing theory-informed chemical kinetics models. *Prog. Energy Combust. Sci.* **2021**, *83*, 100886.

(39) Sivaramakrishnan, R.; Bross, D. H.; Burke, M. P.; Elliot, S. N.; Glarborg, P.; Goldsmith, C. F.; Hansen, N.; Jasper, A. W.; Labbe, N. J.; Miller, J. A.; Mulvihill, C. R.; Ruscic, B.; Tao, Y.; Zádor, J.; Klippenstein, S. J. Theory Informed Kinetics (ThInK 1.0) Model for Core Combustion Species. *Spring Technical Meeting of the Eastern States Section of the Combustion Institute* **2024**, *Paper 1A11*, March 10–13, Athens, GA.

(40) ANSYS Chemkin 2022 R1. 29-Nov-2021; Copyright 2022 ANSYS, Inc.

(41) Zhang, F.; Huang, C.; Xie, B.; Wu, X. Revisiting the chemical kinetics of $CH_3 + O_2$ and its impact on methane ignition. *Combust. Flame* **2019**, *200*, 125–134.

(42) Endo, Y. Private communication (2024).

(43) Cho, J.; Mulvihill, C. R.; Klippenstein, S. J.; Sivaramakrishnan, R. Bimolecular Peroxy Radical (RO_2) Reactions and Their Relevance in Radical Initiated Oxidation of Hydrocarbons. *J. Phys. Chem. A* **2023**, *127*, 300–315.

(44) Nguyen, T. L.; McCarthy, M. C.; Stanton, J. F. Relatively Selective Production of the Simplest Criegee Intermediate in a CH_4 / O_2 Electric Discharge: Kinetic Analysis of a Plausible Mechanism. *J. Phys. Chem. A* **2015**, *119*, 7197–7204.

(45) Anglada, J. M.; Olivella, S.; Solé, A. Mechanistic Study of the $CH_3O_2^\bullet + HO_2^\bullet \longrightarrow CH_3O_2H + O_2$ Reaction in the Gas Phase. Computational Evidence for the Formation of a Hydrogen-Bonded Diradical Complex. *J. Phys. Chem. A* **2006**, *110*, 6073–6082.

(46) Nguyen, T. L.; Stanton, J. F. The Reaction of HO_2 and CH_3O_2: CH_3OOH Formed from the Singlet Electronic State Surface. *Atmosphere* **2022**, *13*, 1397.

(47) Ruscic, B.; Bross, D. H. Active Thermochemical Tables (ATcT) Values Based on ver. 1.130 of the Thermochemical Network. Argonne National Laboratory, Lemont, Illinois. Available at `https://ATcT.anl.gov` (accessed on 30 October 2024).

(48) Ruscic, B.; Pinzon, R. E.; von Laszewski, G.; Kodeboyina, D.; Burcat, A.; Leahy, D.; Montoy, D.; Wagner, A. F. Active Thermochemical Tables: thermochemistry for the 21st century. *J. Phys. Conf. Ser.* **2005**, *16*, 561.

(49) Jasper, A. W.; Klippenstein, S. J.; Harding, L. B. Theoretical rate coefficients for the reaction of methyl radical with hydroperoxyl radical and for methylhydroperoxide decomposition. *Proc. Combust. Inst.* **2009**, *32*, 279–286.

(50) Weddle, P. J.; Karakaya, C.; Zhu, H.; Sivaramakrishnan, R.; Prozument, K.; Kee, R. J. Boundary-Layer Model to Predict Chemically Reacting Flow within Heated, High-Speed, Microtubular Reactors. *Int. J. Chem. Kinet.* **2018**, *50*, 473–480.

(51) Tranter, R. S.; Kastengren, A. L.; Porterfield, J. P.; Randazzo, J. B.; Lockhart, J. P. A.; Baraban, J. H.; Ellison, G. B. Measuring flow profiles in heated miniature reactors with X-ray fluorescence spectroscopy. *Proc. Combust. Inst.* **2017**, *36*, 4603–4610.

(52) Stone, D.; Au, K.; Sime, S.; Medeiros, D. J.; Blitz, M.; Seakins, P. W.; Decker, Z.; Sheps, L. Unimolecular decomposition kinetics of the stabilised Criegee intermediates CH_2OO and CD_2OO. *Phys. Chem. Chem. Phys.* **2018**, *20*, 24940–24954.

(53) Guan, Q.; Urness, K. N.; Ormond, T. K.; David, D. E.; Ellison, G. B.; Daily, J. W. The properties of a micro-reactor for the study of the unimolecular decomposition of large molecules. *Int. Rev. Phys. Chem.* **2014**, *33*, 447–487.

(54) Prozument, K.; Barratt Park, G.; Shaver, R. G.; Vasiliou, A. K.; Oldham, J. M.; David, D. E.; Muenter, J. S.; Stanton, J. F.; Suits, A. G.; Barney Ellison, G.; Field, R. W. Chirped-pulse millimeter-wave spectroscopy for dynamics and kinetics studies of pyrolysis reactions. *Phys. Chem. Chem. Phys.* **2014**, *16*, 15739–15751.

(55) Nguyen, T. L.; Lee, H.; Matthews, D. A.; McCarthy, M. C.; Stanton, J. F. Stabilization of the Simplest Criegee Intermediate from the Reaction between Ozone and Ethylene: A High-Level Quantum Chemical and Kinetic Analysis of Ozonolysis. *J. Phys. Chem. A* **2015**, *119*, 5524–5533.

(56) Caravan, R. L. et al. The reaction of hydroxyl and methylperoxy radicals is not a major source of atmospheric methanol. *Nat. Commun.* **2018**, *9*, 4343.

(57) Nguyen, T.-N.; Putikam, R.; Lin, M. C. A novel and facile decay path of Criegee intermediates by intramolecular insertion reactions via roaming transition states. *J. Chem. Phys.* **2015**, *142*, 124312.

(58) Wu, C.-H.; Magers, D. B.; Harding, L. B.; Klippenstein, S. J.; Allen, W. D. Reaction Profiles and Kinetics for Radical–Radical Hydrogen Abstraction via Multireference Coupled Cluster Theory. *J. Chem. Theory Comput.* **2020**, *16*, 1511–1525.

(59) Burke, M. P.; Klippenstein, S. J. Ephemeral collision complexes mediate chemically termolecular transformations that affect system chemistry. *Nat. Chem.* **2017**, *9*, 1078–1082.

(60) Lakshmanan, S.; Hase, W. L.; Smith, G. P. Mechanism and kinetics for the reaction of methyl peroxy radical with O_2. *Phys. Chem. Chem. Phys.* **2021**, *23*, 23508–23516.

(61) Suenram, R.; Lovas, F. Dioxirane. Its Synthesis, Microwave Spectrum, Structure, and Dipole Moment. *J. Am. Chem. Soc.* **1978**, *100*, 5117–5122.

(62) Prozument, K.; Baraban, J. H.; Changala, P. B.; Park, G. B.; Shaver, R. G.; Muenter, J. S.; Klippenstein, S. J.; Chernyak, V. Y.; Field, R. W. Photodissociation transition states characterized by chirped pulse millimeter wave spectroscopy. *Proc. Natl. Acad. Sci. U.S.A.* **2020**, *117*, 146–151.

(63) Chambreau, S. D.; Townsend, D.; Lahankar, S. A.; Lee, S. K.; Suits, A. G. Novel molecular elimination mechanism in formaldehyde photodissociation: the roaming H atom pathway. *Phys. Scripta* **2005**, *73*, C89.

(64) Sims, I. R.; Smith, I. W. M. Gas-Phase Reactions and Energy Transfer at Very Low Temperatures. *Annu. Rev. Phys. Chem.* **1995**, *46*, 109–138.

(65) Georgievskii, Y.; Klippenstein, S. J. Strange Kinetics of the $C_2H_6 + CN$ Reaction Explained. *J. Phys. Chem. A* **2007**, *111*, 3802–3811.

(66) Shannon, R. J.; Blitz, M. A.; Goddard, A.; Heard, D. E. Accelerated chemistry in the reaction between the hydroxyl radical and methanol at interstellar temperatures facilitated by tunnelling. *Nat. Chem.* **2013**, *5*, 745–749.

(67) Suits, A. G. Roaming Reactions and Dynamics in the van der Waals Region. *Annu. Rev. Phys. Chem.* **2020**, *71*, 77–100.

(68) Zaleski, D. P.; Sivaramakrishnan, R.; Weller, H. R.; Seifert, N. A.; Bross, B., D. H. amd Ruscic; Moore III, K. B.; Elliott, S. N.; Copan, A. V.; Harding, L. B.; Klippenstein, S. J.; Field, R. W.; Prozument, K. Substitution Reactions in the Pyrolysis of Acetone Revealed through a Modeling, Experiment, Theory Paradigm. *J. Am. Chem. Soc.* **2021**, *143*, 3124–3142.

(69) Zaleski, D. P.; Prozument, K. Pseudo-equilibrium geometry of HNO determined by an E-Band CP-FTmmW spectrometer. *Chem. Phys. Lett.* **2017**, *680*, 101–108.

(70) Seifert, N. A.; Ruscic, B.; Sivaramakrishnan, R.; Prozument, K. The C_2H_4O isomers in the oxidation of ethylene. *J. Mol. Spectrosc.* **2023**, *398*, 111847.

(71) Hays, B. M.; Guillaume, T.; Hearne, T. S.; Cooke, I. R.; Gupta, D.; Abdelkader Khedaoui, O.; Le Picard, S. D.; Sims, I. R. Design and performance of an E-band chirped pulse spectrometer for kinetics applications: OCS–He pressure broadening. *J. Quant. Spectrosc. Radiat. Transf.* **2020**, *250*, 107001.

(72) Neill, J. L.; Harris, B. J.; Steber, A. L.; Douglass, K. O.; Plusquellic, D. F.; Pate, B. H. Segmented chirped-pulse Fourier transform submillimeter spectroscopy for broadband gas analysis. *Opt. Express* **2013**, *21*, 19743–19749.

(73) Zaleski, D. P.; Neill, J. L.; Muckle, M. T.; Seifert, N. A.; Brandon Carroll, P.; Widicus Weaver, S. L.; Pate, B. H. A K_a-band chirped-pulse Fourier transform microwave spectrometer. *J. Mol. Spectrosc.* **2012**, *280*, 68–76.

(74) Arenas, B. E.; Gruet, S.; Steber, A. L.; Giuliano, B. M.; Schnell, M. Chirped-pulse Fourier transform millimeter-wave spectroscopy of ten vibrationally excited states of i-propyl cyanide: exploring the far-infrared region. *Phys. Chem. Chem. Phys.* **2017**, *19*, 1751–1756.

(75) Zaleski, D. P.; Duan, C.; Carvajal, M.; Kleiner, I.; Prozument, K. The broadband rotational spectrum of fully deuterated acetaldehyde (CD_3CDO) in a CW supersonic expansion. *J. Mol. Spectrosc.* **2017**, *342*, 17–24.

(76) Hearne, T. S.; Abdelkader Khedaoui, O.; Hays, B. M.; Guillaume, T.; Sims, I. R. A novel Ka-band chirped-pulse spectrometer used in the determination of pressure broadening coefficients of astrochemical molecules. *J. Chem. Phys.* **2020**, *153*, 084201.

TOC Graphic

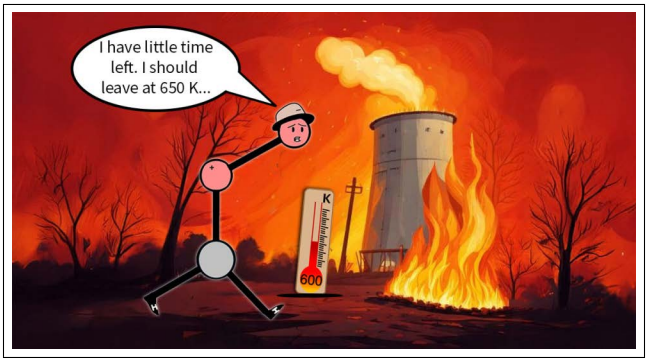

Supporting Information: Thermally-Initiated Formation of Criegee Intermediate CH_2OO in the Oxidation of Ethane

Rizalina T. Saragi,[†] Nathan A. Seifert,[†,‡] Raghu Sivaramakrishnan,[†] and Kirill Prozument[*,†]

†*Chemical Sciences and Engineering Division, Argonne National Laboratory, Lemont, IL, 60439, USA*

‡*Department of Chemistry and Chemical & Biomedical Engineering, University of New Haven, West Haven, CT 06516, USA*

E-mail: prozument@anl.gov

The Journal of Physical Chemistry Letters
2024

Contents

List of Tables

List of Figures

Signal Calibration

The integrated intensities of lines in Figures 1–3 and S1–S5 were calibrated to account for i) the excitation and detection efficiency of the spectrometer and ii) the chirping bandwidth. Chirps were brought to a linear regime by 60 dB attenuation of the mmW and their amplitudes were measured using an oscilloscope (Tektronix DPO73304DX). The calibrated intensities in Table S1 were obtained by dividing the integrated line intensities by the chirps' amplitudes and multiplied by $\sqrt{\Delta\nu}$. The relative abundances are found using the PGOPHER program to simulate the line intensities using the published dipole moments and rotational constants of the molecules of interest. The rotational temperature of every species is assumed to be 5 K (see the relative line intensities in the acetaldehyde spectrum in Fig. S2). Finally, the mole fractions in the mixture were found using a reference stable molecule $CH_2DC^{13}CH$. A mixture of 5% (by mole) propyne in argon (without O_2) flowed through the reactor at $T_{wall} = 1500$ K. We measured the spectrum of the $CH_2DC^{13}CH$ isotopologue of propyne in natural abundance (Fig. S6). We assume that its absolute abundance is the product of the parent mole fraction (0.05), the natural abundance of D (0.000145) and the natural abundance of ^{13}C (0.0106), i.e. 7.685×10^{-8}. With that, the absolute abundances (mole fractions) of the reaction intermediates can be adjusted in a PGOPHER simulation to match the observed ratios of their calibrated line intensities to that of $CH_2DC^{13}CH$.

Kinetic Modeling

The in-house kinetic model, ThInK, was simulated on a 0-D homogeneous reactor on Chemkin with the following conditions: 1800 K, 1.0 atm, 5% C_2H_6 and 5% O_2 in Ar, and for 200 μs. Simulations at the same conditions over the first 5 μs provide insight into the early-time kinetics. Figure S7 shows the mole fractions of the key stable molecules and radicals involved in ethane oxidation as a function of time. Figures S8–S24 show the rate of production of related species and their most significant reactions in the scope of the ThInK model.

Table S1: List of Frequency

Species	Transition			Exp. Freq (MHz)	Intensity	Ref. Freq	Ref.
CH_2OO	$3_{03} - 2_{02}$			69420.641(20)	13.14	69420.6536	JPL [a]
CH_2OO	$3_{13} - 2_{12}$			66922.355(50)	3.29	66922.3880	JPL
CH_2OO	$3_{12} - 2_{11}$			72152.081(50)	4.37	72152.0559	JPL
CH_2OO	$4_{14} - 3_{13}$			89189.583(100)	2.40	89189.6346	JPL
CH_3OOH	$4_{04} - 3_{03}$	0^+ [b]		77747.001(20)	9.35	77747.0549	JPL
CH_3OOH	$4_{04} - 3_{03}$	0^-		77765.113(100)	0.64	77765.1582	JPL
CH_3OOH	$4_{13} - 3_{12}$	0^+		81008.643(50)	5.05	81008.6484	JPL
HO_2	$1_{01} - 0_{00}$	3/2 - 1/2 [c]	1−0 [d]	65070.862(20)	1443.44	65070.85(8)	JPL
HO_2	$1_{01} - 0_{00}$	3/2 - 1/2	2−1	65081.787(20)	3725.25	65081.82(4)	JPL
HO_2	$1_{01} - 0_{00}$	3/2 - 1/2	1−1	65098.487(20)	306.93	65098.44(9)	JPL
HO_2	$1_{01} - 0_{00}$	1/2 - 1/2	1−0	65373.006(20)	526.16	65373.01(10)	JPL
HO_2	$1_{01} - 0_{00}$	1/2 – 1/2	0−1	65396.186(20)	796.26	65396.15(10)	JPL
HO_2	$1_{01} - 0_{00}$	1/2 – 1/2	1−1	65400.616(20)	108.74	65400.63(10)	JPL
CH_3CHO	$4_{04} - 3_{03}$	A		76866.440(20)	1081.98	76866.4357	JPL
CH_3CHO	$4_{04} - 3_{03}$	E		76878.958(20)	1329.74	76878.9525	JPL
CH_3CHO	$4_{23} - 3_{22}$	A		77038.620(20)	165.18	77038.6010	JPL
CH_3CHO	$4_{22} - 3_{21}$	A		77218.314(20)	242.70	77218.2910	JPL

Species	Transition		Exp. Freq (MHz)	Intensity	Ref. Freq	Ref.
CH_3CHO	$4_{22} - 3_{21}$	E	77125.653(20)	127.34	77125.6950	JPL
CH_3CHO	$4_{23} - 3_{22}$	E	77126.482(20)	132.64	77126.4134	JPL
syn-CH_2CHOH	$4_{04} - 3_{03}$		77726.552(20)	52.30	77726.58	Rodler and Bauder[e]
syn-CH_2CHOH	$6_{06} - 5_{15}$		76840.808(50)	9.93	76840.77	Rodler and Bauder[e]
anti-CH_2CHOH	$4_{04} - 3_{03}$		77361.141(50)	11.07	77361.12	Rodler[f]
C_2H_5CHO	$8_{18} - 7_{17}$		77182.023(50)	18.21	77181.9857(400)	CDMS[g]
C_2H_5CHO	$8_{08} - 7_{07}$		77952.179(50)	34.43	77181.9857(400)	CDMS
trans-HCOOH	$3_{13} - 2_{12}$		64936.254(20)	35.95	69436.2747(16)	CDMS
trans-HCOOH	$3_{03} - 2_{02}$		67291.116(20)	62.00	67291.1296(15)	CDMS
trans-HCOOH	$3_{12} - 2_{11}$		69851.947(20)	44.20	69851.9640(16)	CDMS
cis-HCOOH	$3_{13} - 2_{12}$		63799.487(50)	5.02	63799.4934(27)	CDMS
cis-HCOOH	$3_{13} - 2_{12}$		68014.132(100)	3.29	68014.0927(31)	CDMS
cis-HCOOH	$1_{10} - 1_{01}$		76175.302(100)	4.65	76175.3218(31)	CDMS
cis-HCOOH	$3_{03} - 2_{02}$		65840.319(50)	5.59	65840.1982(29)	CDMS
cis-HCOOH	$3_{03} - 2_{02}$		65840.334(50)	4.57	65840.1982(29)	CDMS
c-C_2H_4O	$2_{02} - 1_{11}$		63558.705(20)	16.56	63558.7070(3)	CDMS
c-C_2H_4O	$2_{12} - 1_{01}$		67776.852(20)	61.82	67776.8575(3)	CDMS
c-C_2H_4O	$4_{13} - 4_{04}$		65822.539(50)	5.14	65822.5467(4)	CDMS

Species	Transition	Exp. Freq (MHz)	Intensity	Ref. Freq	Ref.
$CH_2DC^{13}CH$	$4_{04} - 3_{03}$	62775.821(50)	2.83	62775.7946(50)	CDMS

[a]Jet Propulsion Laboratory (https://spec.jpl.nasa.gov/).

[b]Inversion.

[c]$J'-J$.

[d]$F'-F$.

[e]*J. Am. Chem. Soc., Vol. 106. No. 14, 1984.*

[f]*J. Mol. Spec., Vol. 114, No. 1, 1985.*

[g]The Cologne Database for Molecular Spectroscopy (https://cdms.astro.uni-koeln.de/).

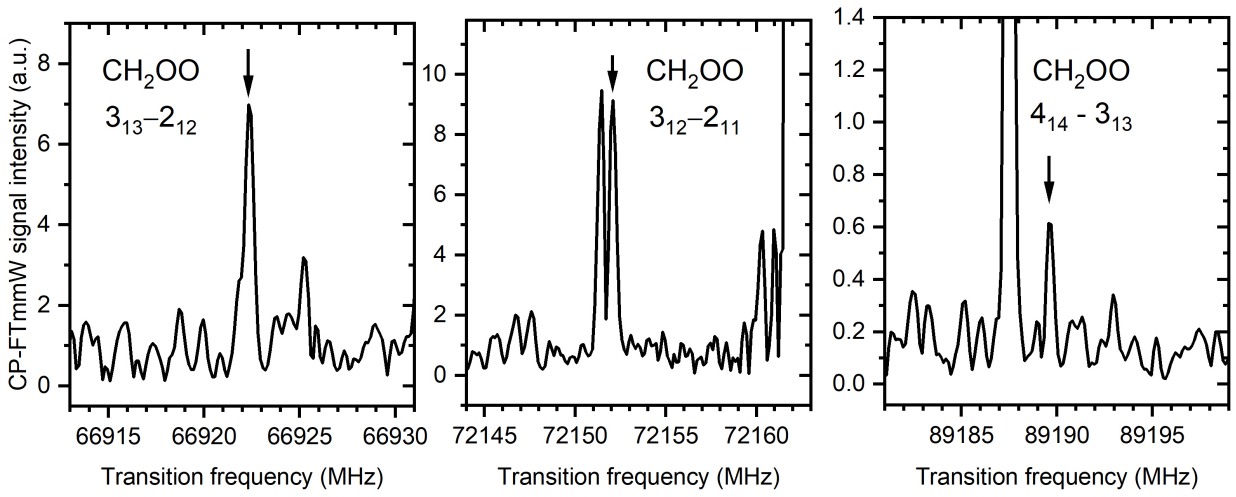

Figure S1: The rotational spectra of CH_2OO formed in the oxidation of ethane. The chirp bandwidths are 150 MHz (only 20 MHz portions are shown), and each FID is averaged 100 million.

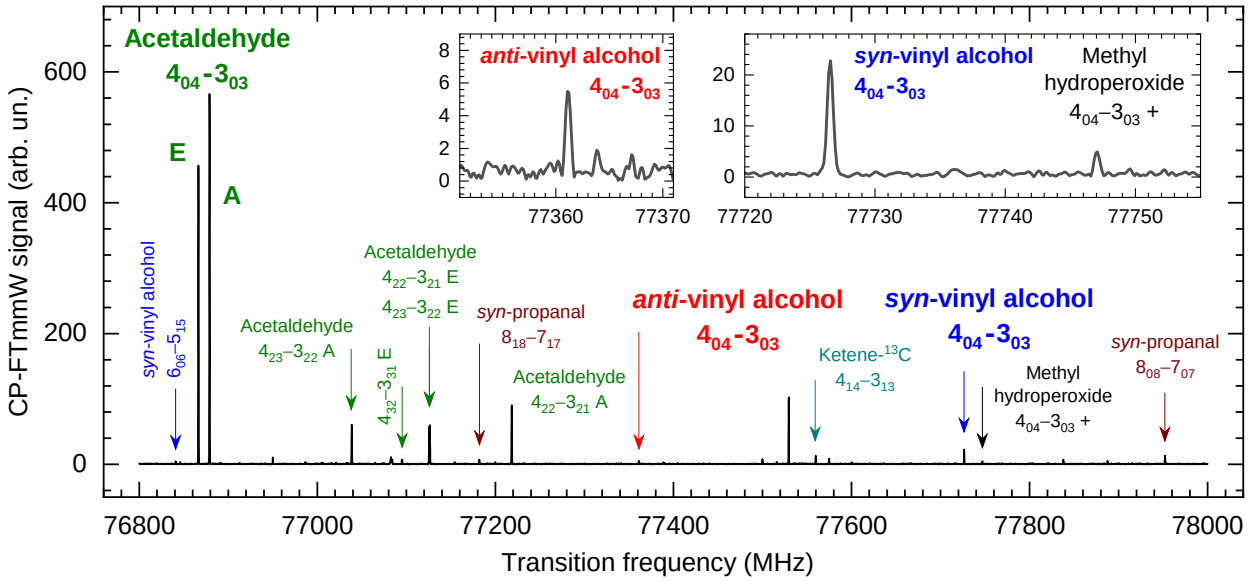

Figure S2: The 76800 – 78000 MHz rotational spectrum of CH_3CHO, *syn*-CH_2CHOH, *anti*-CH_2CHOH, *syn*-C_2H_5CHO (propanal), and other species formed in the oxidation of ethane. The chirp bandwidth is $\Delta\nu$ = 1200 MHz and the LO frequency is 75.6 GHz, resulting in the IF frequency in the 1.2 – 2.4 GHz range. The FID is averaged 100 million times in 10 minutes. The spectral data is available as a separate file in the SI.

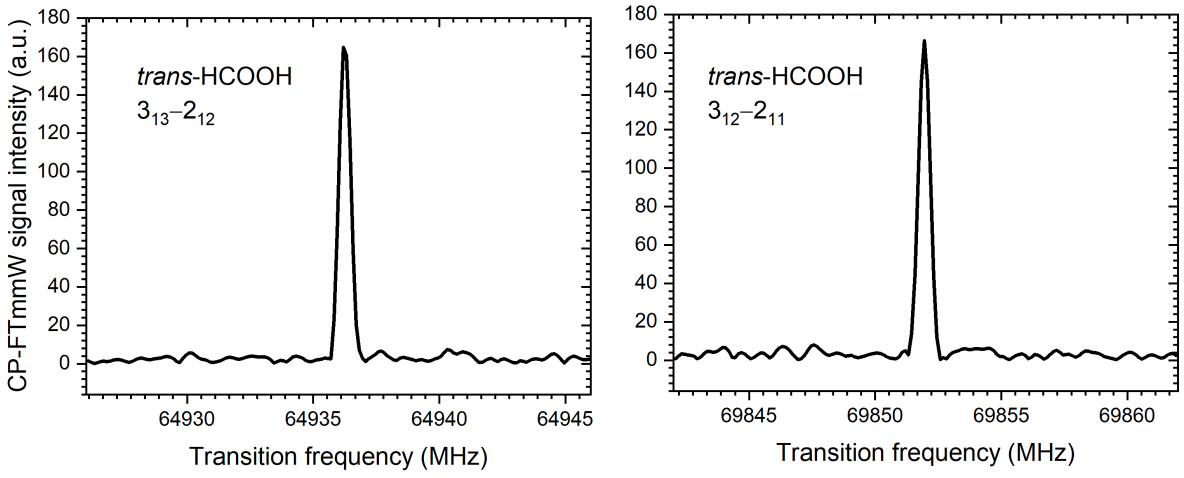

Figure S3: The rotational spectra of *trans*-HCOOH. The chirp bandwidths are 20 MHz, and each FID is averaged 10 million times.

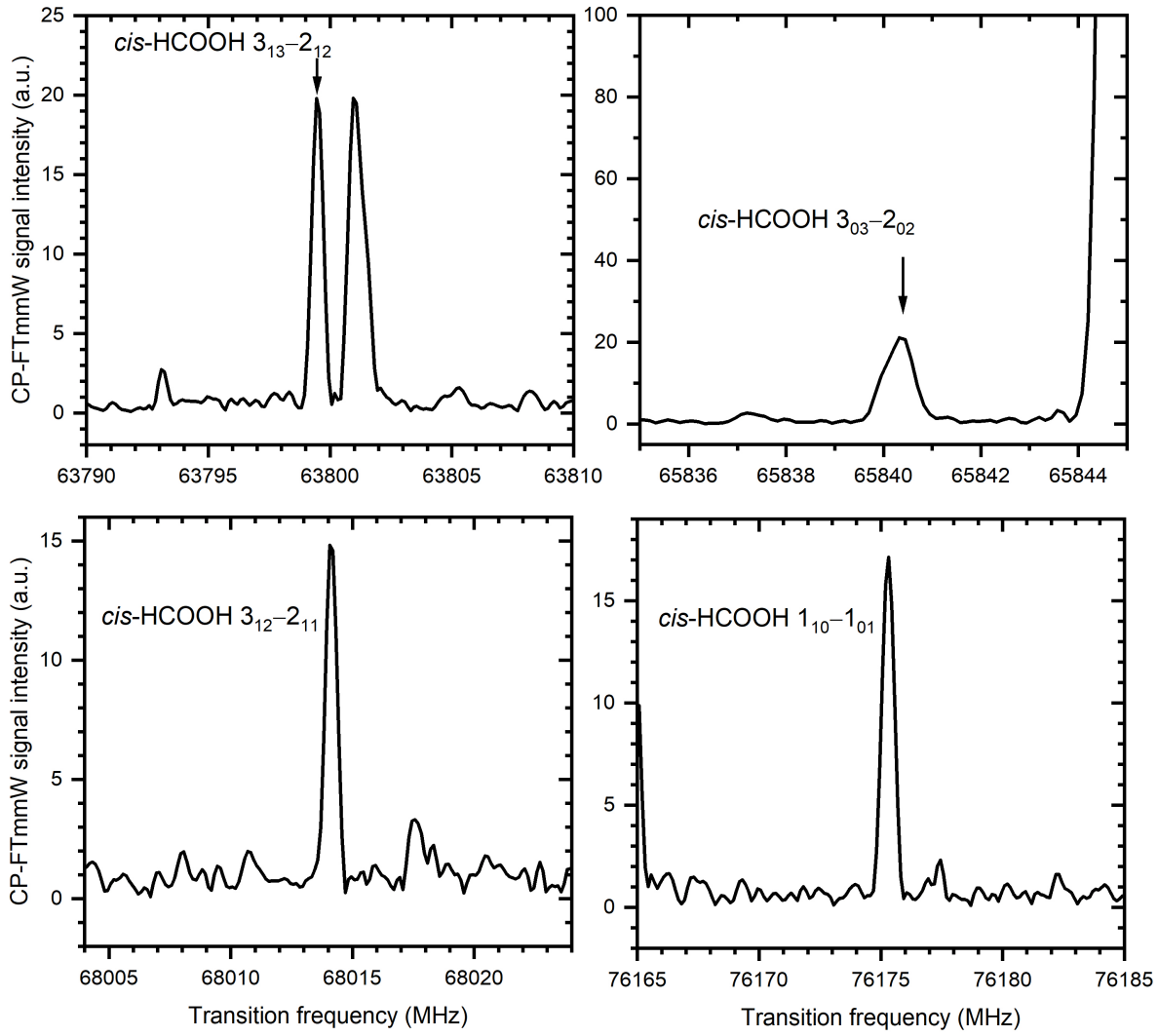

Figure S4: The rotational spectra of *cis*-HCOOH. The chirp bandwidths are 20 MHz, and each FID is averaged 100 million times.

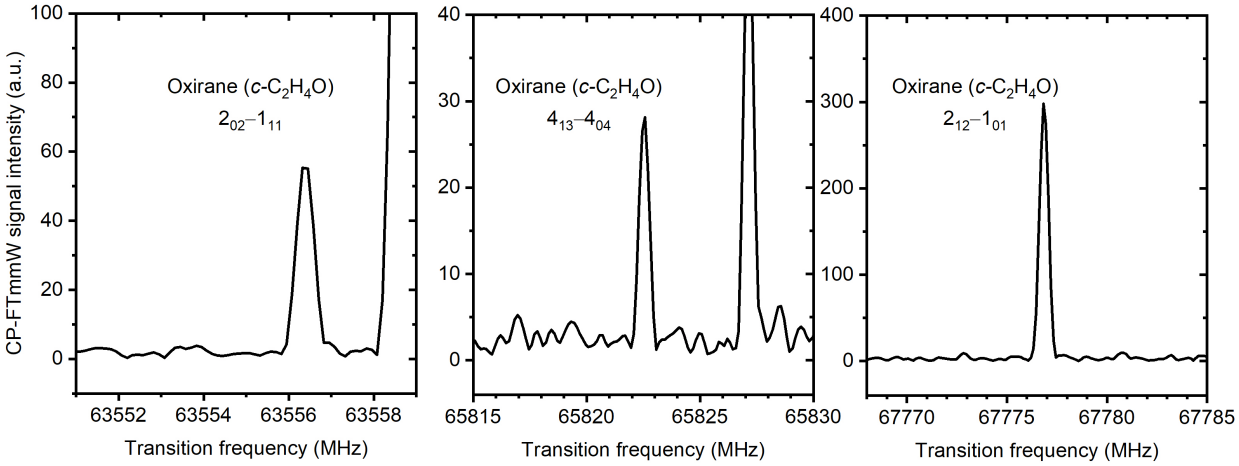

Figure S5: The rotational spectra of oxirane (c-C_2H_4O). The chirp bandwidths are 20 MHz, and each FID is averaged 10 million times.

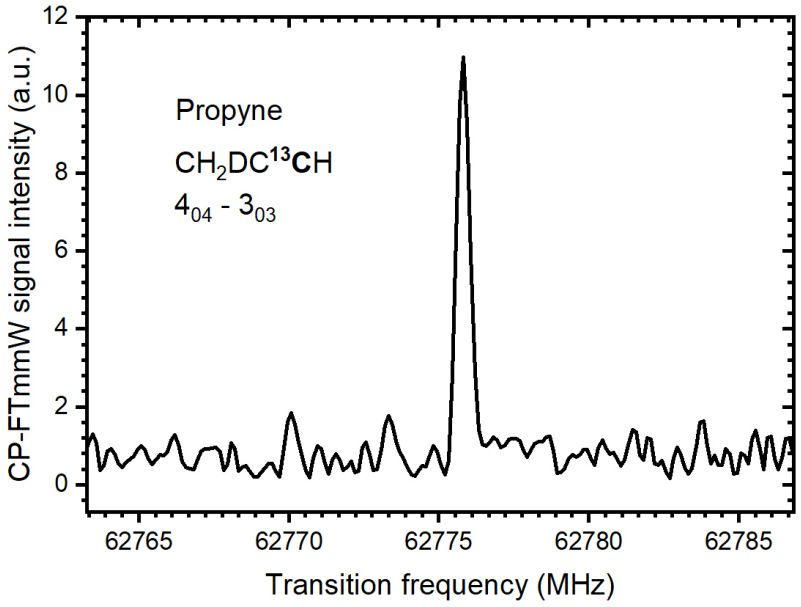

Figure S6: Mole fraction calibration. The rotational spectrum of $CH_2DC^{13}CH$. The chirp bandwidth is 30 MHz, and the FID is averaged 100 million times in 10 minutes. LO frequency is 60.8 GHz. In this measurement, a sample of 5% propyne in argon (without O_2) flows at $Q = 2000$ sccm through the reactor heated to $T_{wall} = 1500$ K, and $CH_2DC^{13}CH$ is detected in natural abundance.

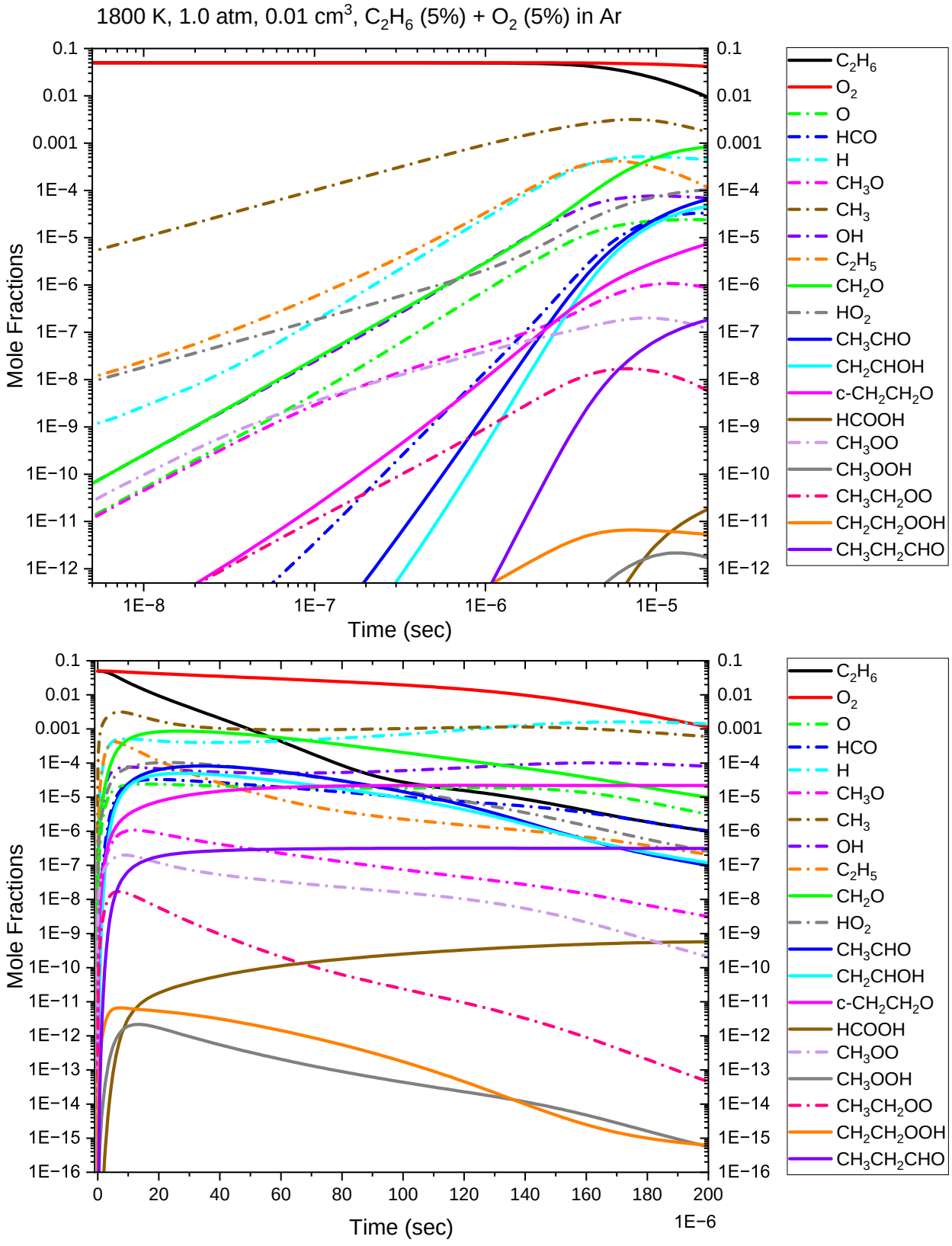

Figure S7: Mole fractions of some intermediates in the oxidation of ethane. Early time formation (upper panel) and evolution during the residence time in the microreactor (lower panel).

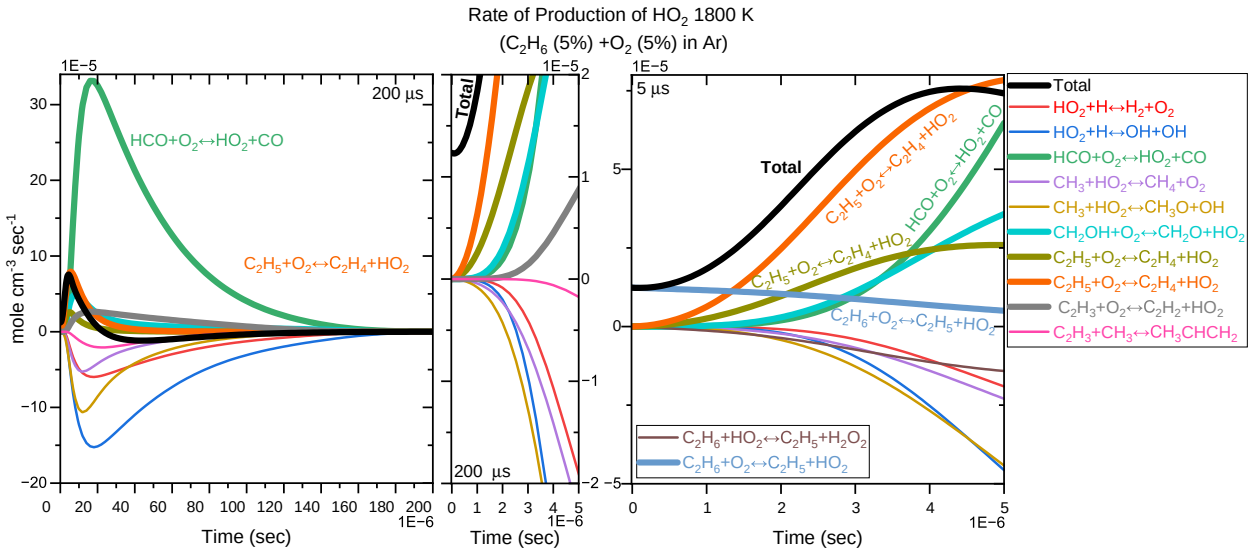

Figure S8: Rate of Production of HO_2 for 5 μs and 200μs.

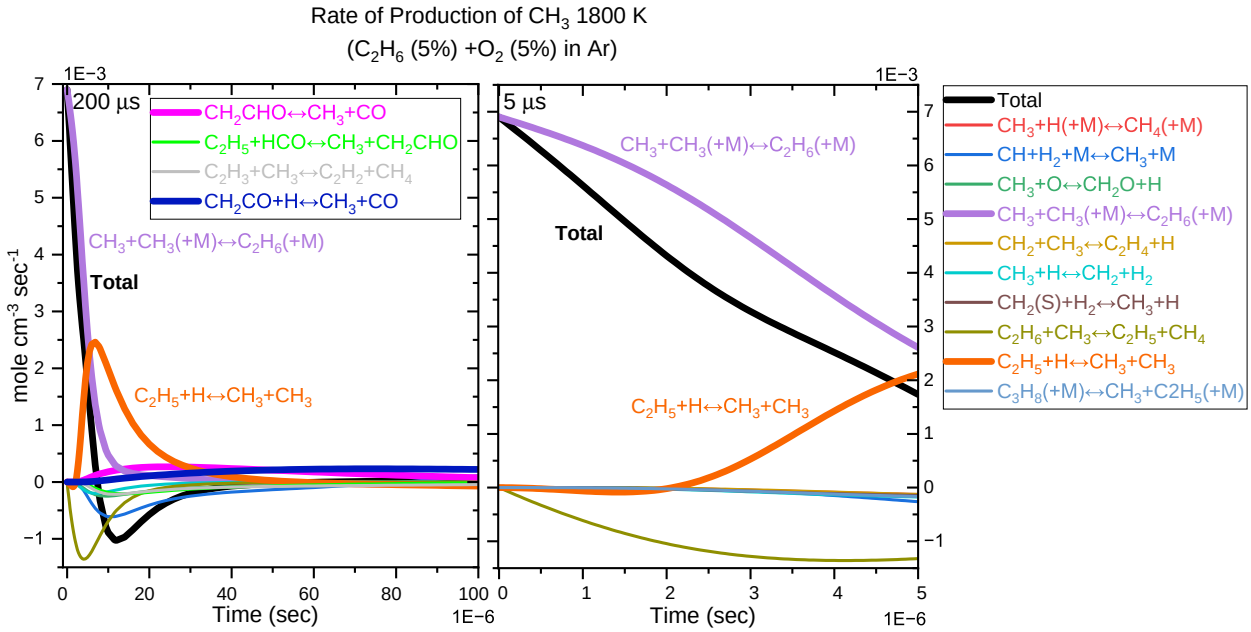

Figure S9: Rate of Production of CH_3 for 5 μs and 200μs .

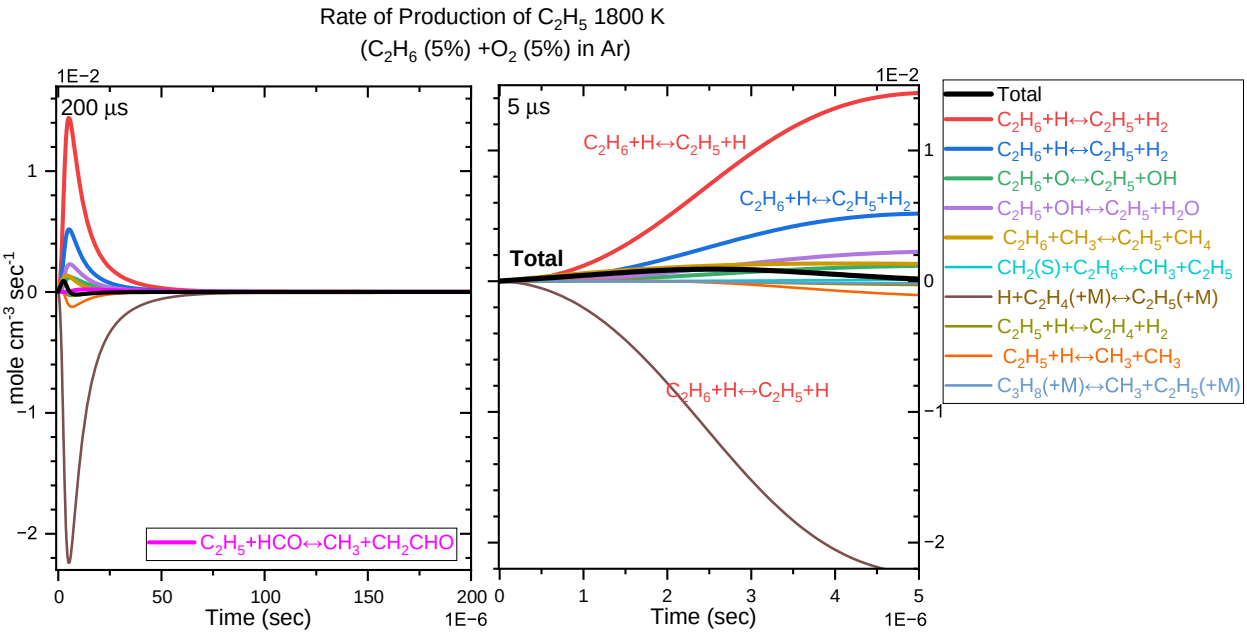

Figure S10: Rate of Production of C_2H_5 for 5 μs and 200μs .

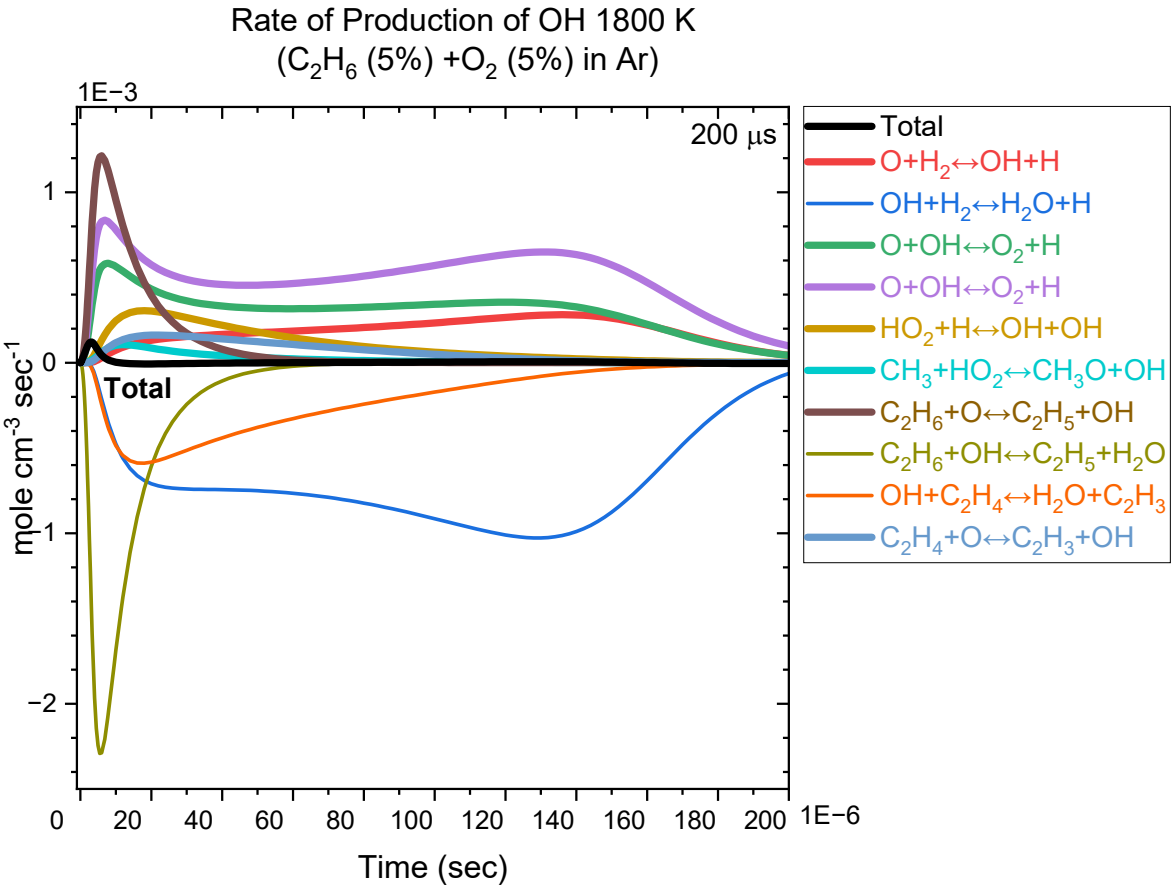

Figure S11: Rate of Production of OH for 200μs .

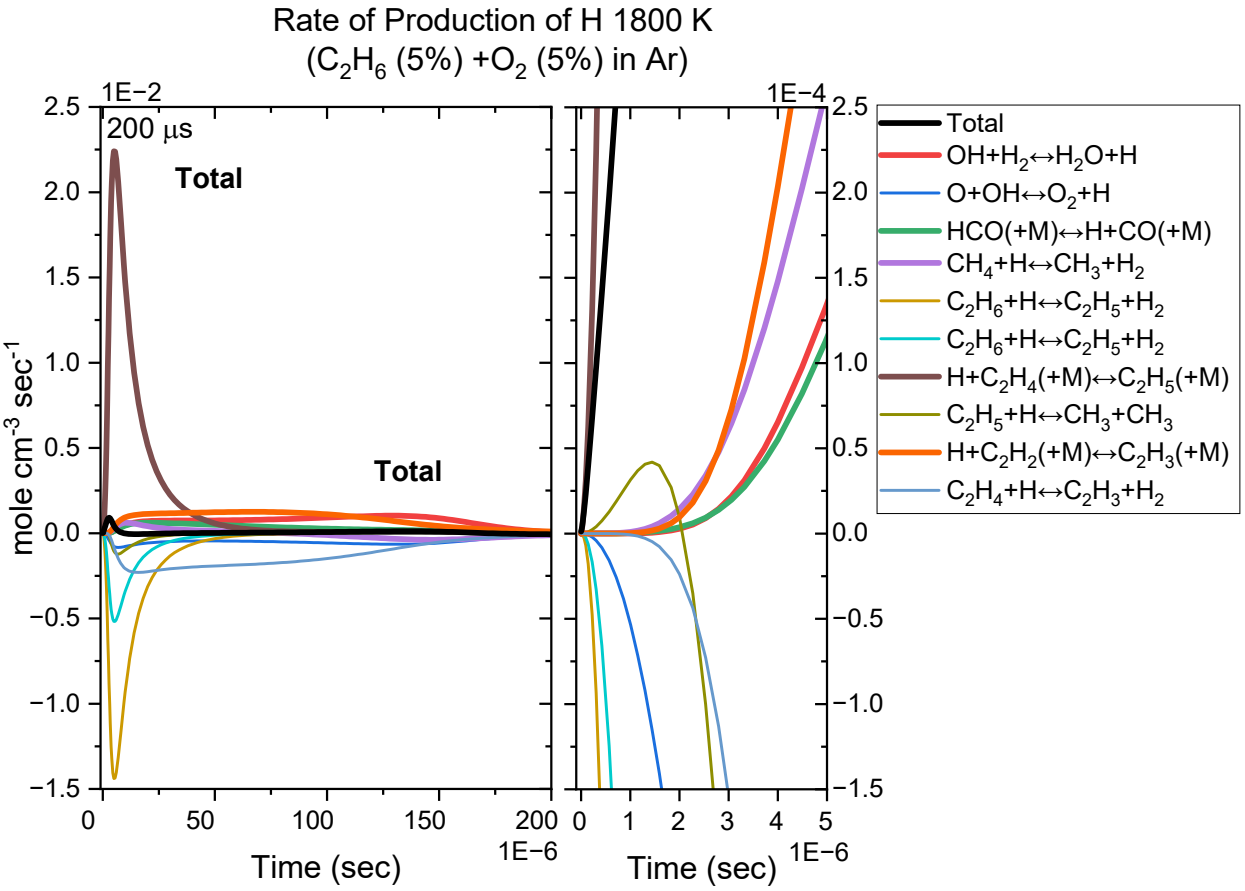

Figure S12: Rate of Production of H for 200μs .

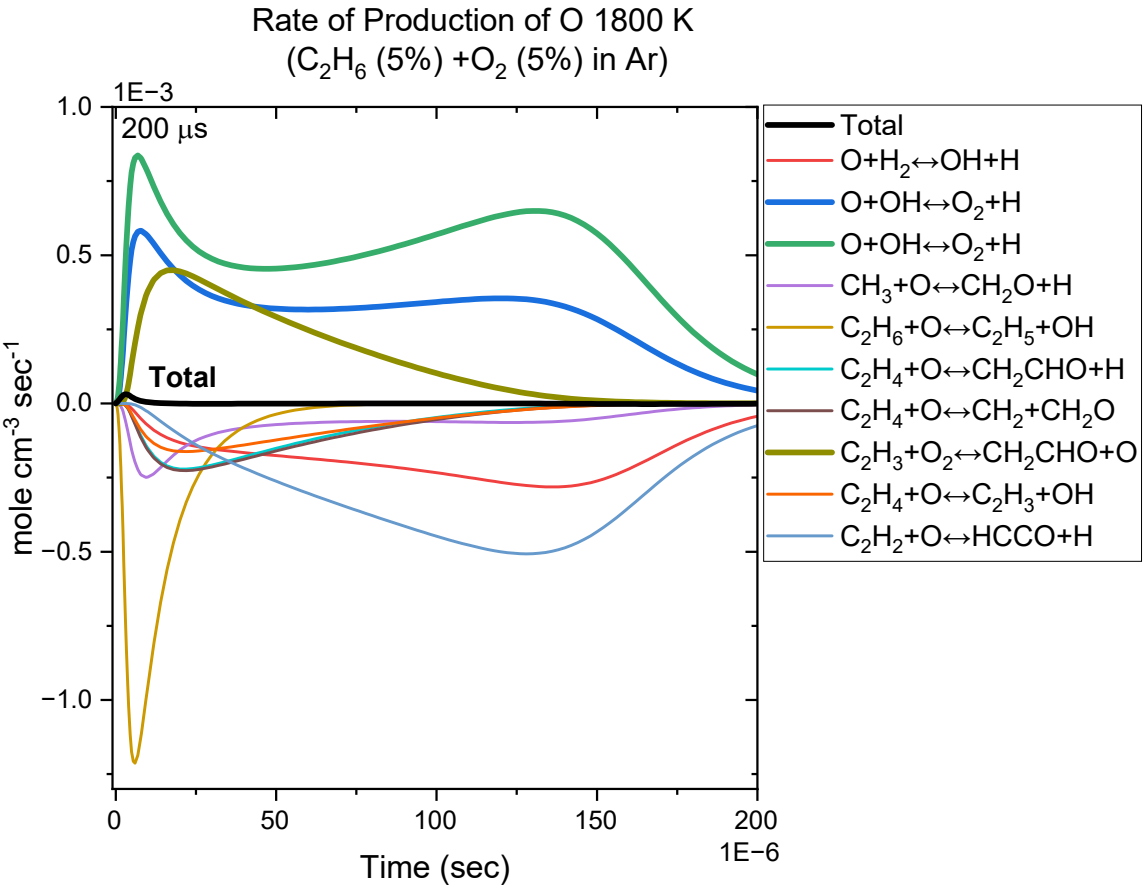

Figure S13: Rate of Production of O for 200μs .

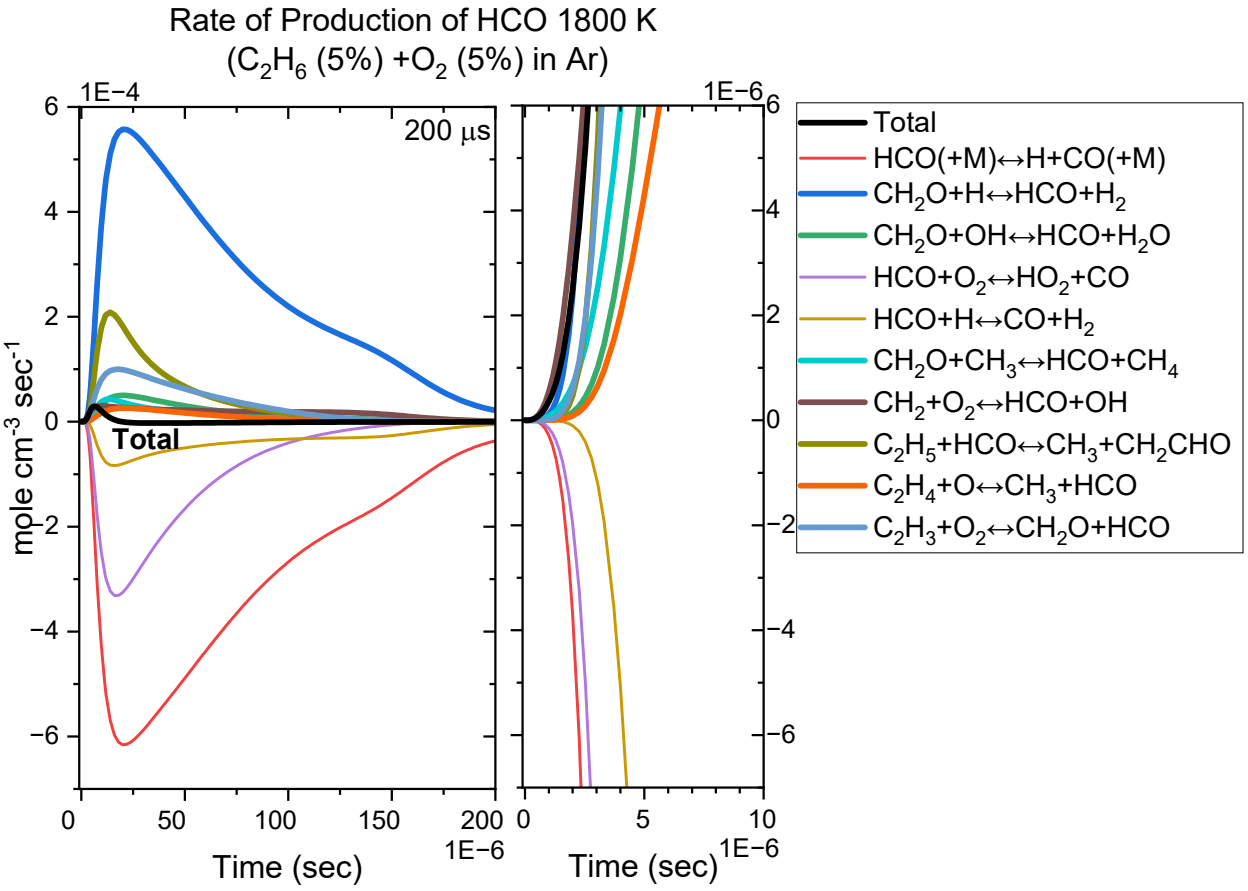

Figure S14: Rate of Production of HCO for 200μs .

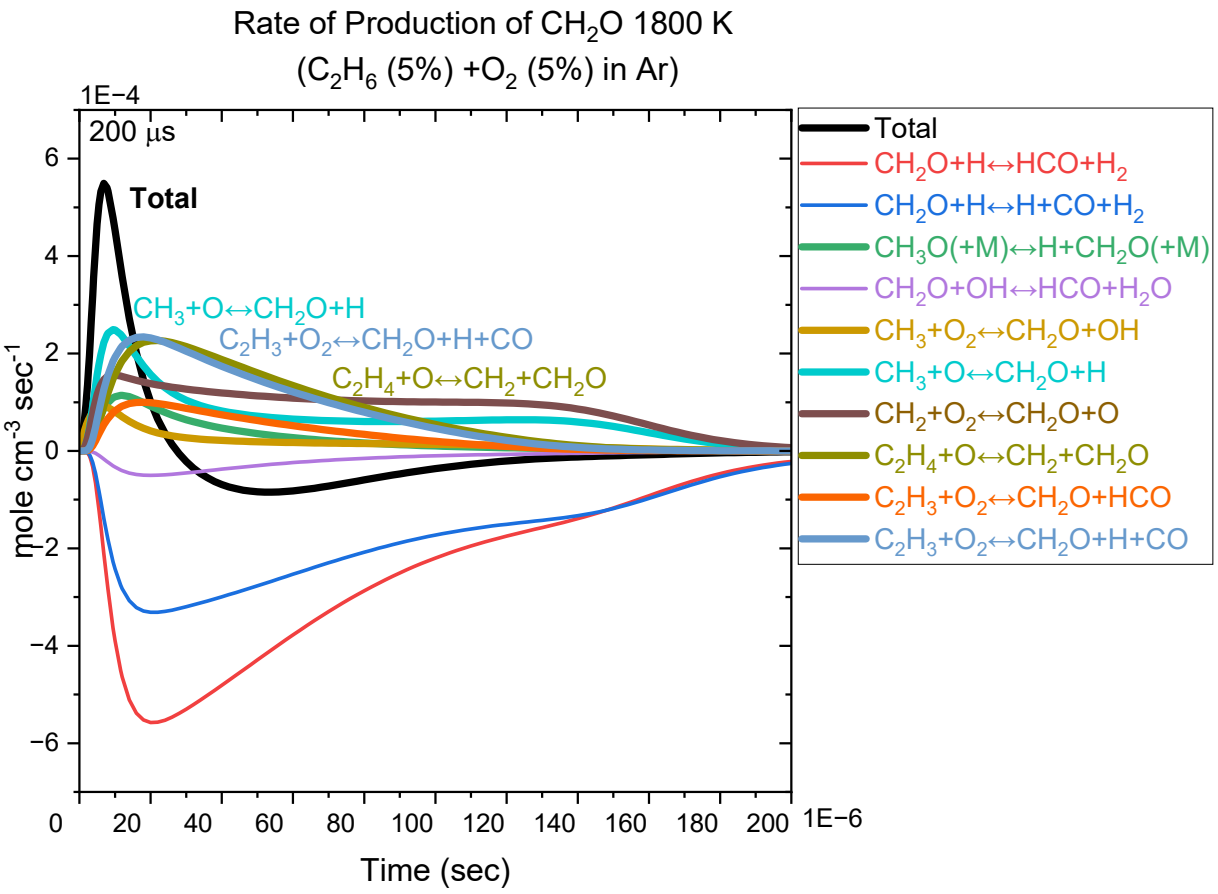

Figure S15: Rate of Production of CH_2O for 200μs .

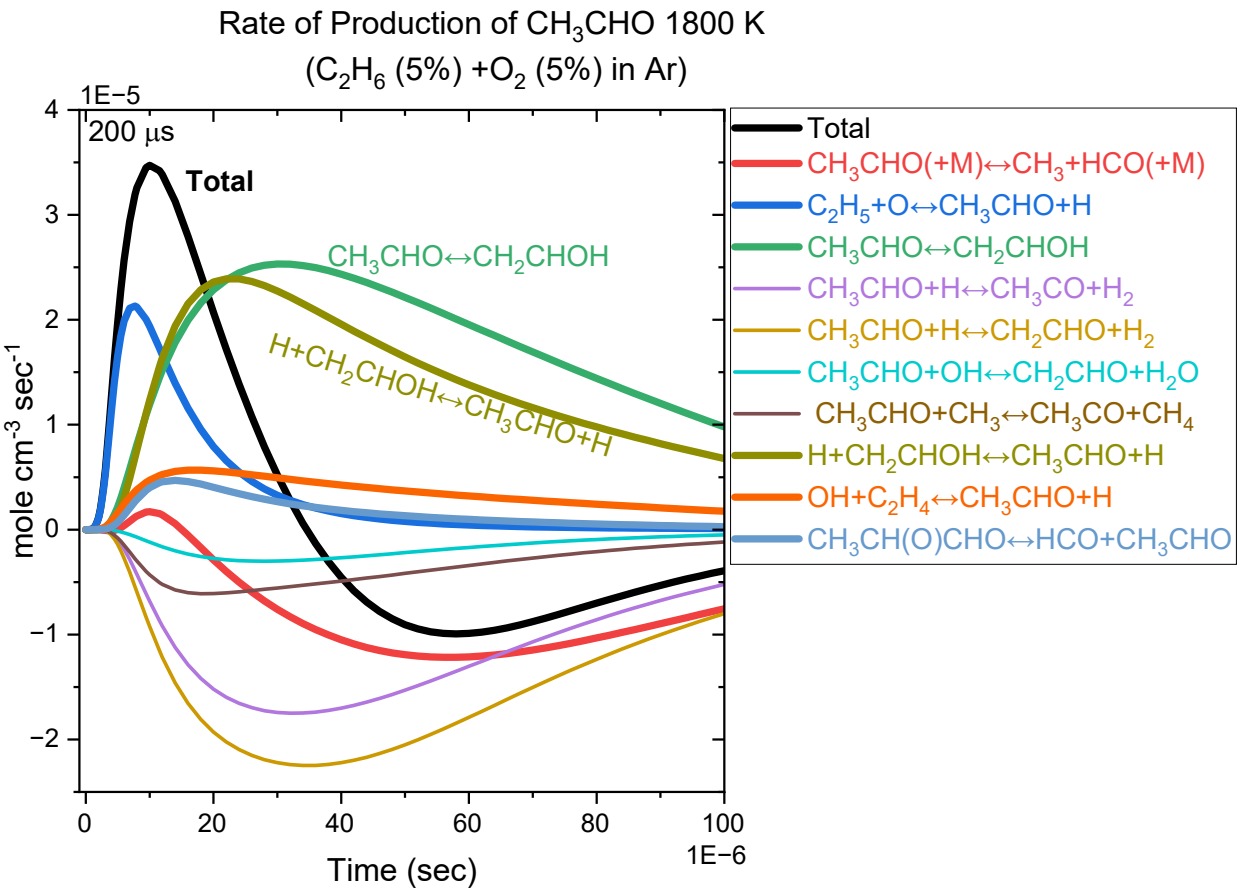

Figure S16: Rate of Production of CH_3CHO for 200μs .

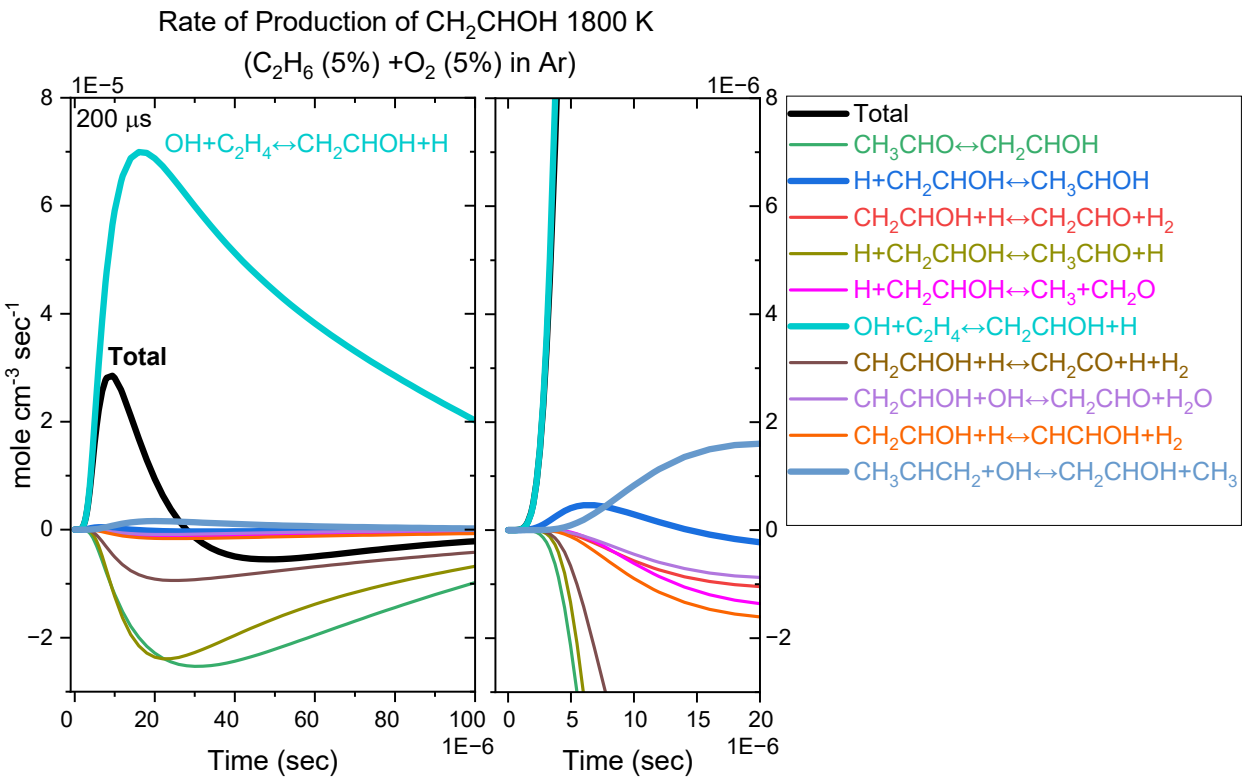

Figure S17: Rate of Production of CH_2CHOH for 200μs .

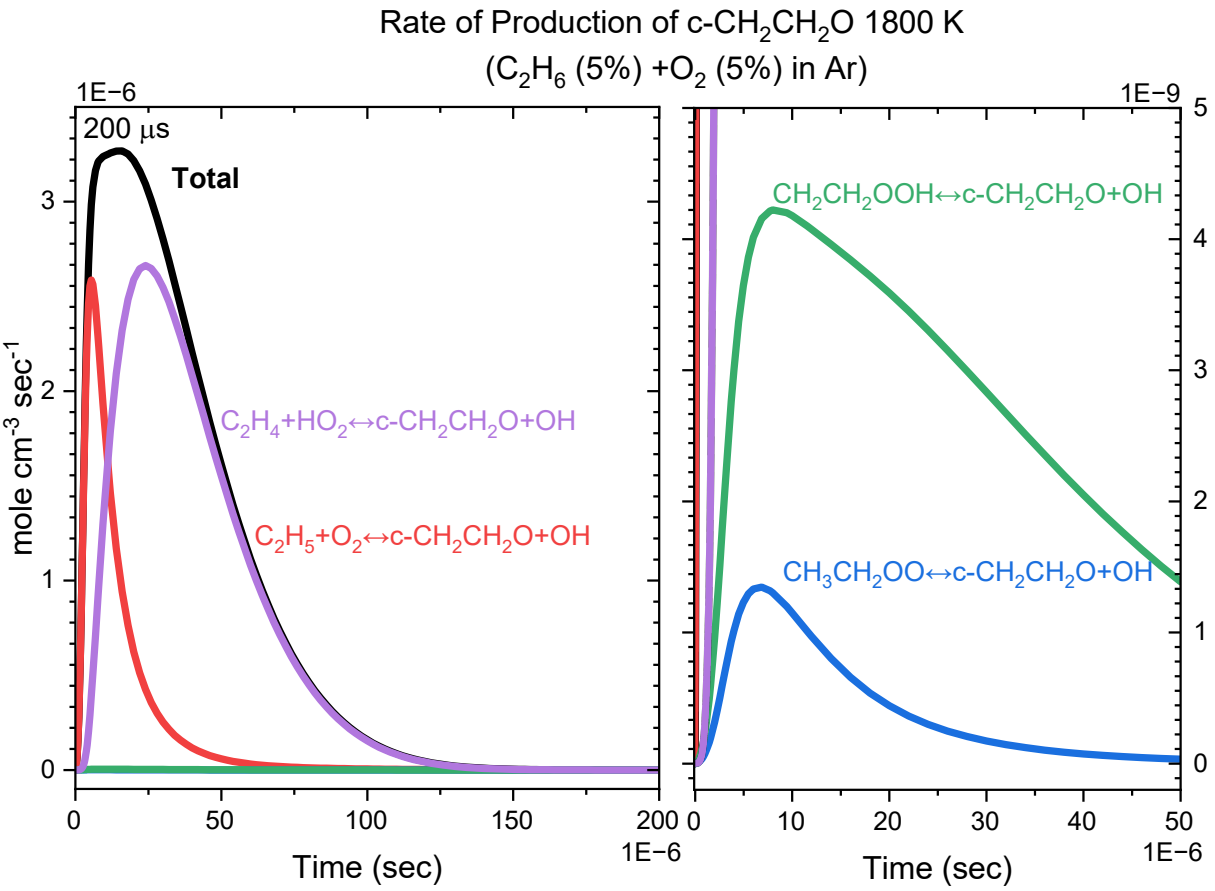

Figure S18: Rate of Production of c$-CH_2CH_2O$ for 200μs .

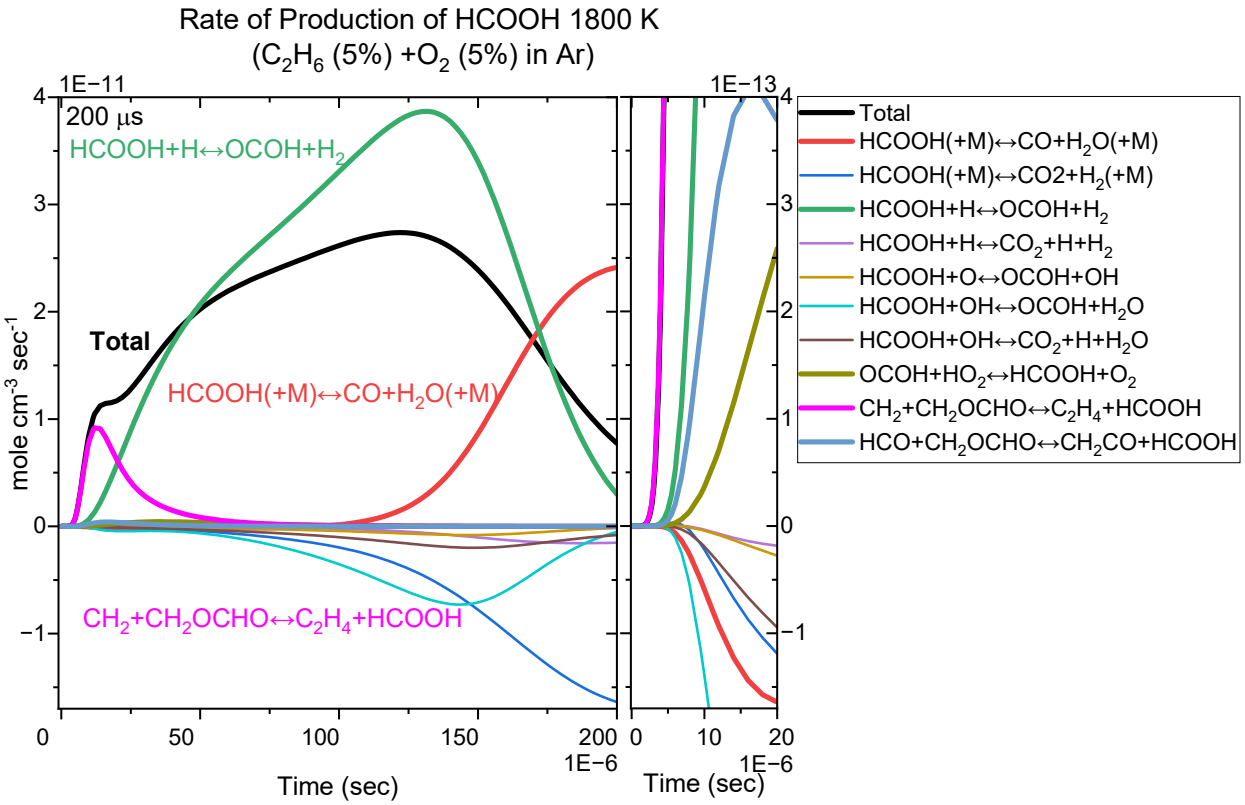

Figure S19: Rate of Production of HCOOH for 200μs .

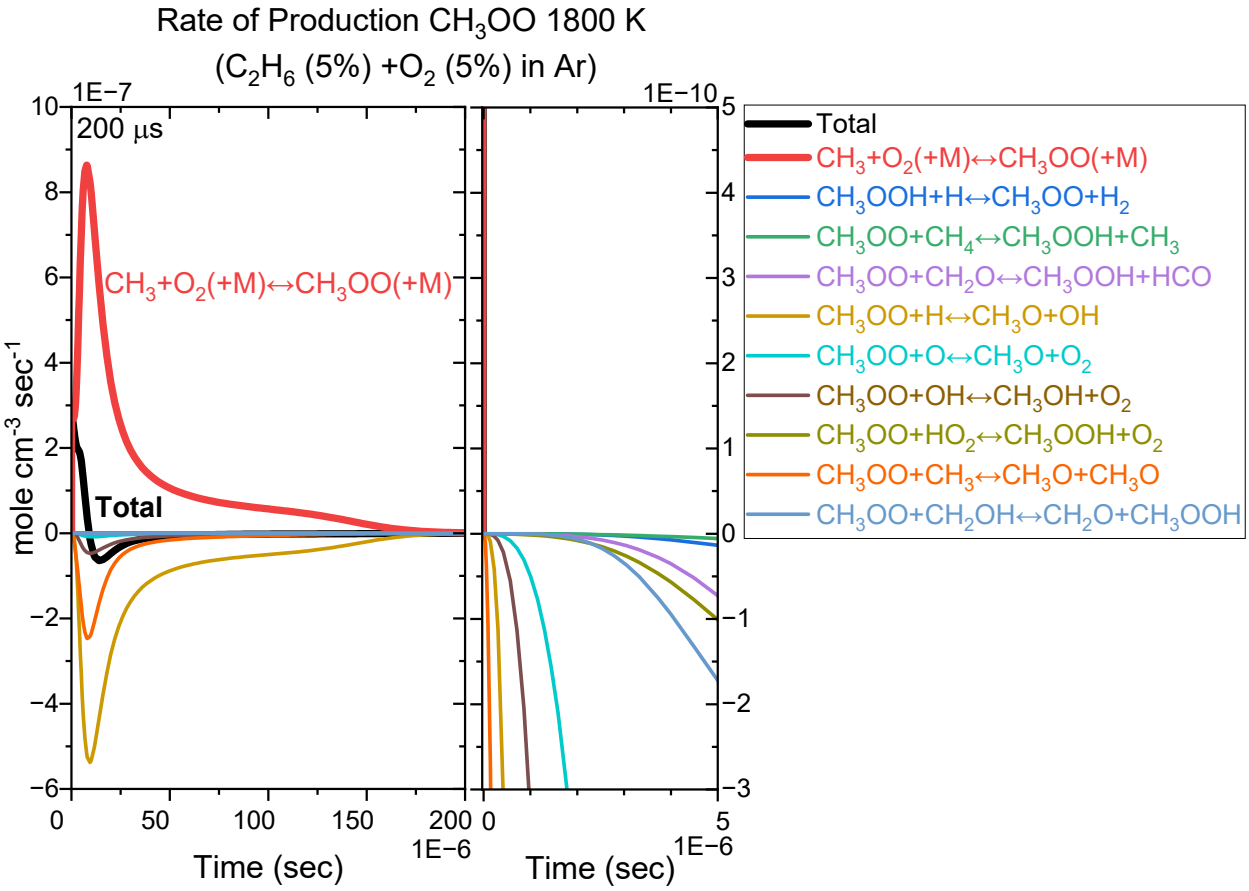

Figure S20: Rate of Production of CH_3OO for 200μs .

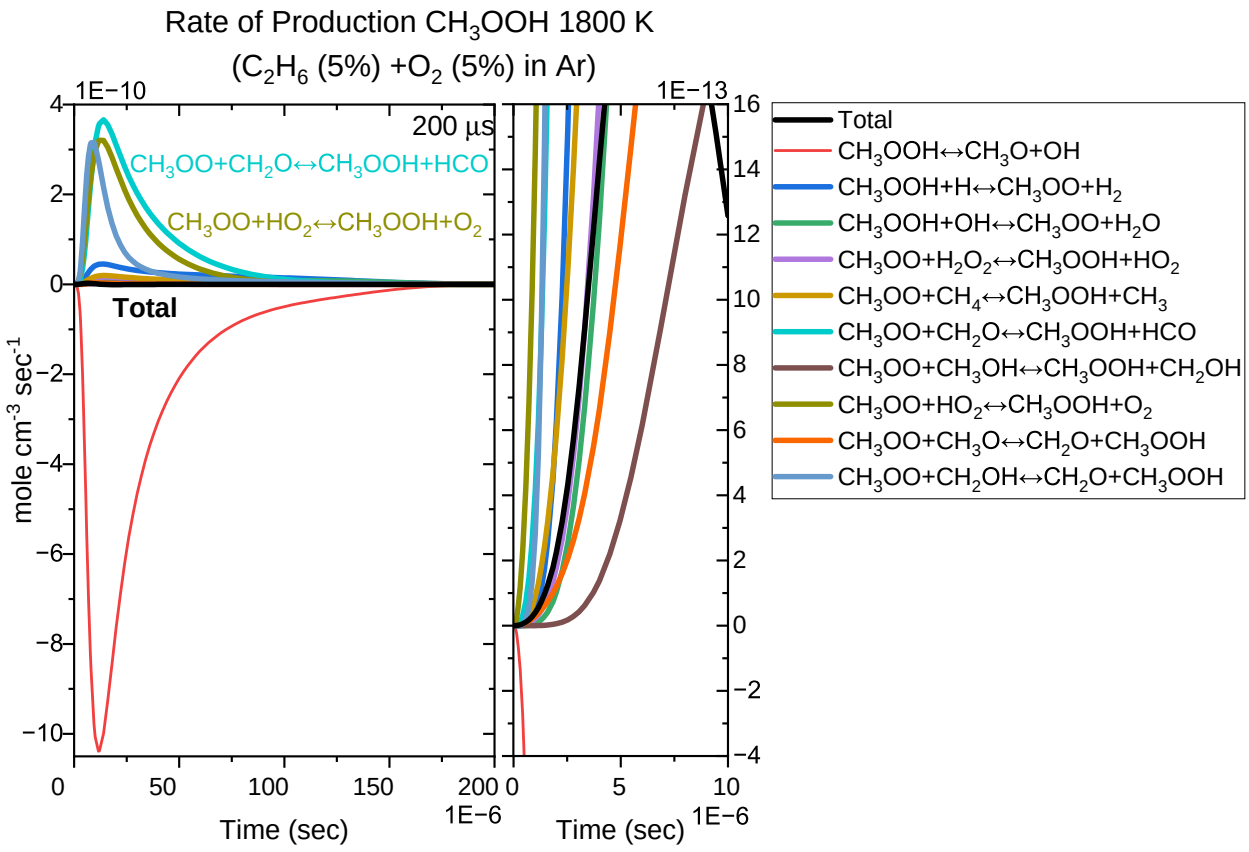

Figure S21: Rate of Production of CH_3OOH for 200μs .

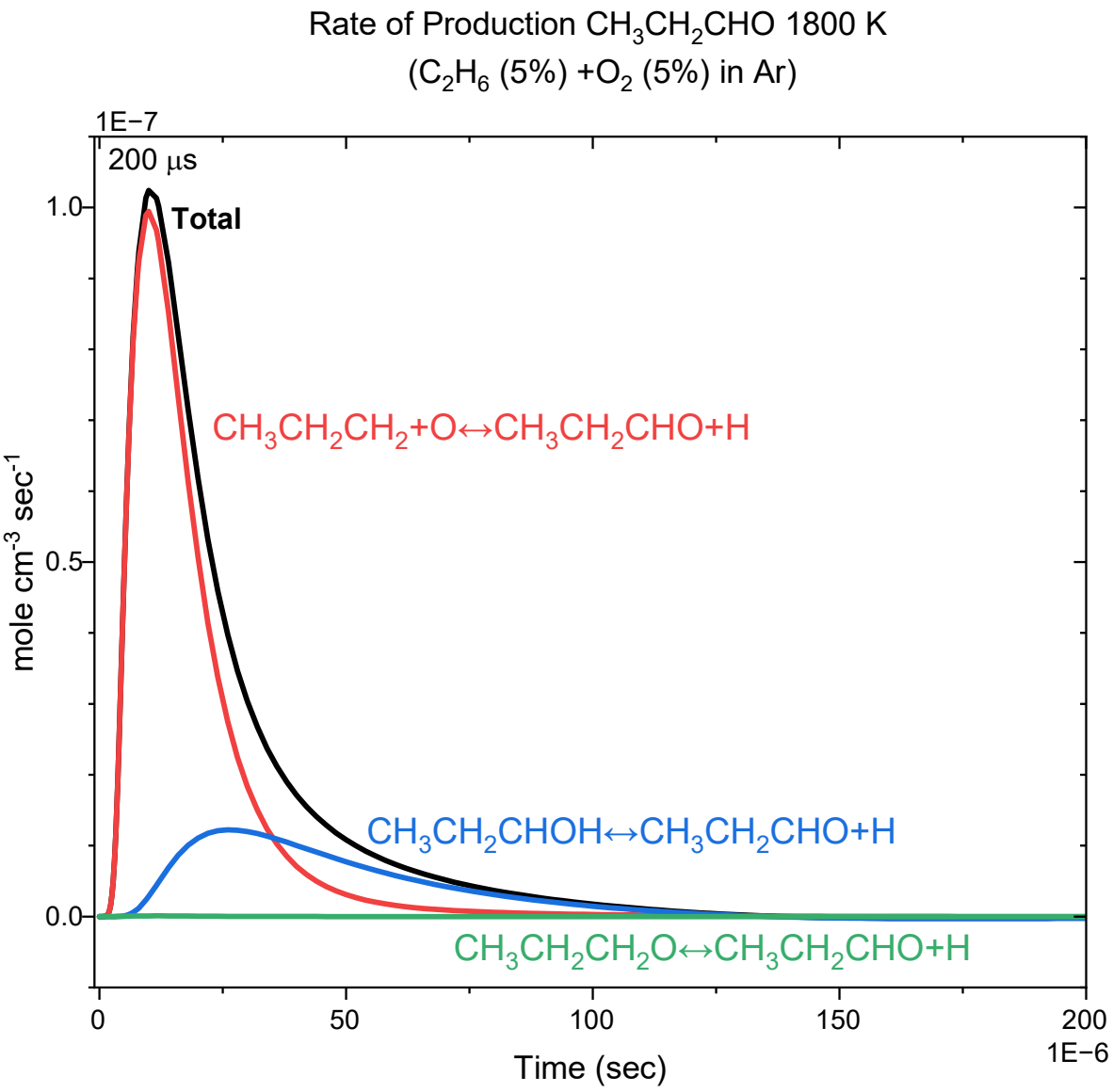

Figure S22: Rate of Production of C_2H_5CHO for 200μs .

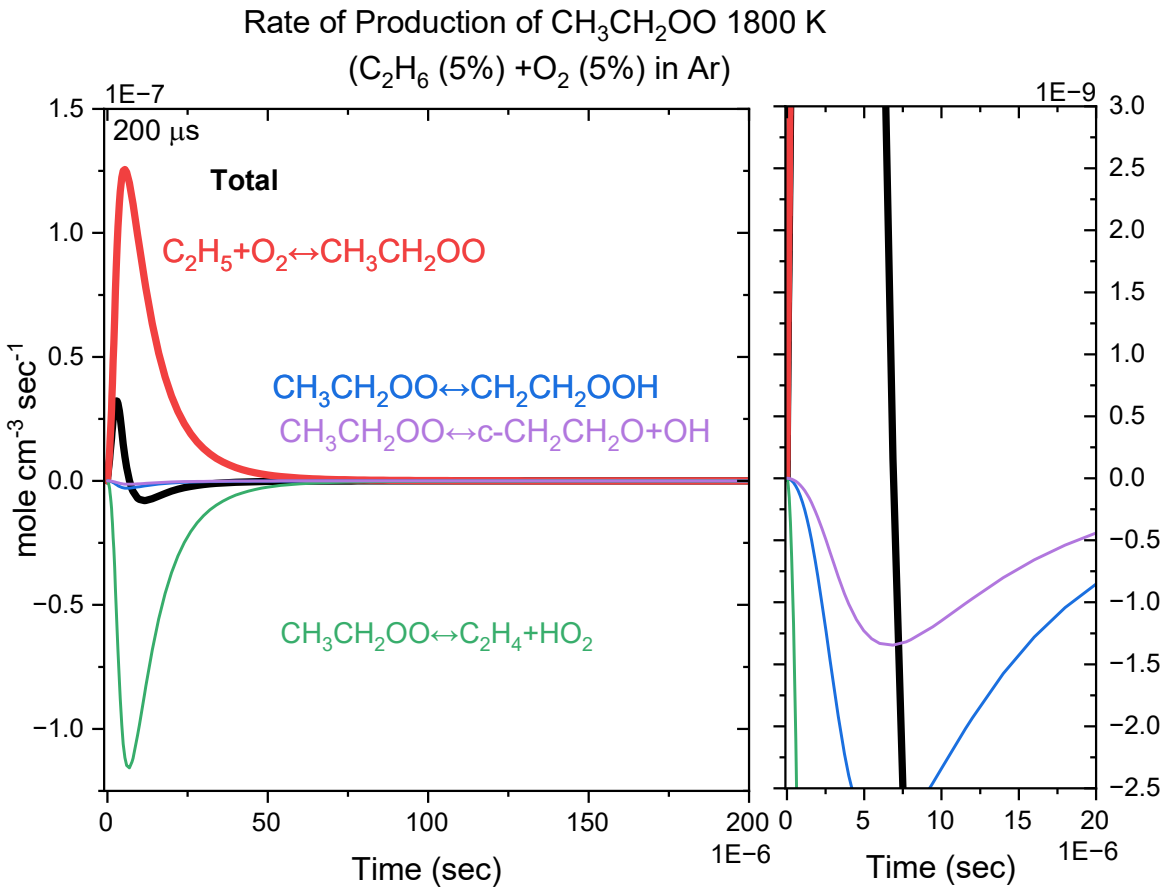

Figure S23: Rate of Production of CH_3CH_2OO for 200μs .

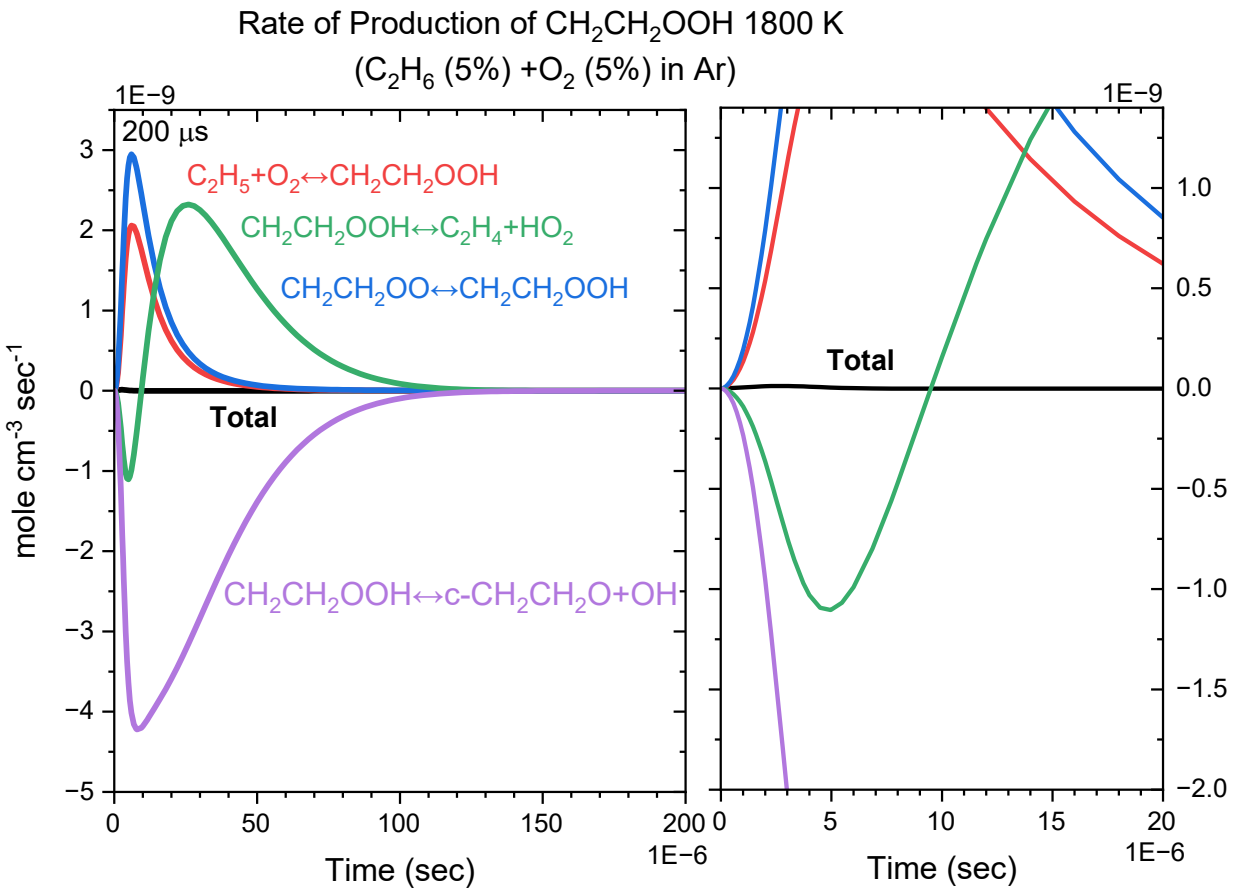

Figure S24: Rate of Production of CH_2CH_2OOH for 200μs .